Check for updates

Visibly transparent supercapacitors

S. Kiruthika, [ID] *[a] Namuni Sneha [ID] [a] and Ritu Gupta [ID] *[b]

Supercapacitors with novel functionalities such as transparency and flexibility are gaining attention to meet the increasing demand for intelligent and smart electronics. Transparent supercapacitors (TSCs) find application in modern appliances such as portable electronics and are especially inevitable for fully integrated transparent devices, thanks to their high-power density, fast charging and discharging ability, and longer life. Transparency is generally achieved by preparing thin films of active electrode material or by adopting lithographic methods for nanostructured electrodes that control the thickness and fill factor without significantly affecting intrinsic conductivity and capacitance. This review discusses all such approaches with a focus on the choice of electrode materials and their design and fabrication for achieving visible transparency in supercapacitors for advanced multifunctional devices. Additionally, it covers the basic concept, device structures, critical parameters, and figure of merit used specifically for transparent supercapacitors. An overview of recent experimental attempts to explore the potential applications of transparent supercapacitors is given, along with the challenges foreseen for the development.

1. Introduction

The emerging demand for transparent optoelectronic devices urges technological innovations that lead to high optical transmittance without sacrificing performance.[1,2] Transparent technology provides more visual information about electronic gadgets than conventional non-transparent ones.[3,4] An enormous effort has been made to transform non-transparent circuits, transistors, and displays to be almost visibly clear.[5–8] Technologically advanced electronic devices can be realized by integrating with transparent energy storage devices.[9] Supercapacitors are new generation energy storage devices for portable electronics due to their compact, low cost, easy processability, higher power densities than batteries, and long cycle life.[10–12] Supercapacitors are an ideal alternative to batteries for low power/energy requirements when there is a need for high power delivery.[13] Energy is stored in electrochemical capacitors either by electrochemical double-layer formation on absorbing ions at the electrode–electrolyte interface or rapid redox

aDepartment of Physics, School of Electrical and Electronics Engineering, SASTRA Deemed to be University, Thanjavur, Tamil Nadu, India. E-mail: kiruthika@ece.sastra.edu

bDepartment of Chemistry, Indian Institute of Technology Jodhpur, India. E-mail: ritu@iitj.ac.in

Dr. S. Kiruthika received her PhD degree (2017) from Jawaharlal Nehru Centre for Advanced Scientific Research, India with DST Inspire Fellowship. After her postdoctoral studies at the Centre for Nano and Soft Matter Sciences, India, she joined as a research scientist (2019) at SASTRA Deemed University, Thanjavur, India. Her research interests include transparent devices, smart energy storage devices, and functional nanomaterials. Currently, she is a visiting scientist at the University of Manchester, UK, supported by SERB-SIRE Grant.
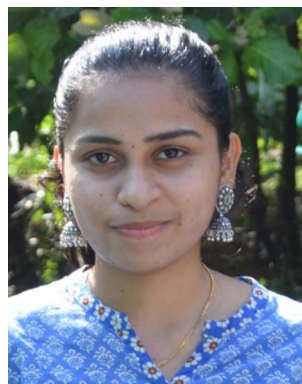
Namuni Sneha received her M. S. degree in Chemistry from Osmania University, India, in 2019. Now, she is pursuing her PhD degree under the supervision of Dr S. Kiruthika at SASTRA Deemed University, India. Her research focuses on chemical engineering and fabrication of metal nanonetworks, and their functional applications towards flexible energy devices.

reactions (pseudo-capacitive).[14] The device performance has been improved by developing novel nanostructured materials with sub-nanometer pores for future systems such as hybrid electric vehicles and industrial equipment.[8] Since the specific capacitance of a conventional supercapacitor depends on the electrode material's mass, area, or volume, a transparent supercapacitor is still a counterintuitive concept and is nascent. Unlike conventional energy storage devices, transparent supercapacitors are highly adaptable to next-generation flexible transparent electronics, especially in wearable devices, sensors, and health monitors.[15–20] Developing transparent electrodes with excellent optoelectronic properties and electrochemical and mechanical stability is significant for constructing flexible transparent supercapacitors. Besides several evaluation metrics for transparent electrodes, various transparent conducting electrodes used in supercapacitors are summarized. The different strategies for fabricating transparent supercapacitors and their applications are discussed in detail. This investigation of the transparent supercapacitor is a branch of transparent electronics that bridges materials and chemical sciences with information technology.[4] Hence a detailed discussion of the transparent supercapacitor is necessary.

1.1. Device architecture of transparent supercapacitors

A transparent supercapacitor comprises a substrate, current collector, active material, and electrolyte, where all components must be essentially transparent.[4] The term electrode in a supercapacitor generally refers to a combination of the active material, current collector, and substrate. Supercapacitors are classified as film supercapacitors and micro-supercapacitors based on electrode alignment.[21] Unlike typical supercapacitors, transparent devices demand visible transparency from every component involved in fabrication, from active materials, electrolytes, and separators to current collectors,

Prof. Ritu Gupta obtained her PhD from Jawaharlal Nehru Centre for Advanced Scientific Research (JNCASR), Bangalore, in 2013 and completed postdoctoral research at Purdue University, USA. She is Associate Professor at IIT Jodhpur. Her research group focuses on developing functional nanomaterials for electrochemical energy devices and nanosensors for environmental monitoring and healthcare applications. She has received several prestigious awards, and fellowships as a young researcher. She is a recipient of the INSA Young Scientist Medal 2020, SERB Women Excellence Award-2021, IIT Jodhpur Research Excellence Award Medal 2020, and NASI Young Scientist Platinum Jubilee Award 2021. Presently, she is also a visiting faculty at Technion-Israel Institute of Technology, Israel with prestigious SERB-SIRE fellowship.

including packaging.[1] This unique requirement poses a significant challenge in developing transparent energy storage devices as, in general, none are usually transparent except for the electrolyte.[9,22,23] On the other hand, one may have to choose wisely the transparent conducting materials considering various parameters like the figure of merit (FoM), specular and diffusive transmittance, haze, and bandgap other than electrical conductivity.[24–26]

In film supercapacitors, two transparent electrodes have a sandwich configuration with a separator or solid-state gel electrolyte. Based on the operating mechanism, the supercapacitor is symmetric if the active material coated on both electrodes is identical; otherwise, it is denoted as an asymmetric supercapacitor.[27–29] Asymmetric configurations basically have an electric double-layer capacitance (EDLC) electrode and a pseudocapacitance electrode sandwiched with a separator or gel electrolyte. EDLC stores energy *via* the fast and highly reversible electrostatic adsorption/desorption of electrolyte ions onto the electrochemically active and stable electrode as a double layer under applied voltage bias. The more commonly used carbon-based electrode materials like CNTs, graphene, and carbon black are a few EDLC electrodes.[30] Pseudocapacitance stores charges *via* a reversible faradaic charge transfer. The typical examples of pseudocapacitance materials are transition metal oxides (MnO_2 and Co_3O_4), hydroxides ($Ni(OH)_2$), carbides (Ti_3C_2), and sulfides (CuS and MoS_2); conducting polymers like polyaniline (PANI) and polypyrrole (PPy).[21,31] Furthermore, the electrode should possess a high specific surface area for fast ion/electron transfer for superior performance of storage devices.[4]

On the other hand, planar 2D printed micro-supercapacitors (MSCs) have recently received much interest because of their excellent stability towards deformations, high electrochemical performance, and ease of on-chip integration with various flexible and functional electronic devices. MSCs have a substantially longer working lifetime, around 100 000 cycles, a faster charging/discharging rate, and a higher power density than flexible batteries. Micro-supercapacitors have attracted attention for applications such as implanted biochips and sensors as they satisfy the demands like long cycle life, quick charge–discharge capability, and high-power density.[32]

1.2. Evaluation metrics

An ideal transparent electrode for an energy storage device should possess low sheet resistance ($R_S \sim 10$ Ω sq^{-1}), high transmittance ($T \sim 90\%$), and high capacitance. For a material to be transparent in the visible region of the electromagnetic spectrum (400–700 nm), it must have a bandgap > 3.1 eV (400 nm).[33] Typically, insulators have a bandgap of 3–5 eV, whereas oxide-based conductors usually show a high bandgap (>3 eV).[34] In a semiconductor with a filled valence band and an empty conduction band, band gaps are around 2 eV.[35] The electrode transmittance is calculated at 550 nm in the UV-visible spectrum, and sheet resistance can be obtained using two or four-probe geometry.[4] More commonly, electrodes with high transmittance are realized by reducing the thickness of active

4908 | *J. Mater. Chem. A*, 2023, **11**, 4907–4936

This journal is © The Royal Society of Chemistry 2023

materials, which, in turn, significantly affects the sheet resistance, which reduces the capacitance. Therefore, there is always a trade-off between these two parameters.[36] To avoid difficulty in direct comparison, a few performance metrics are derived for easy evaluation of TCE performance. When it comes to the commercial aspects of the device, the chemical and mechanical stabilities of electrodes, their associated cost, and stability towards deformation should also be deeply considered.[37]

1.2.1. Capacitive figure-of-merit (FoMc) for transparent supercapacitors. The figure of merit for a transparent conductor is specified as in eqn (1) and (2):[38]

$$T = \left(1 + \frac{Z_o}{2R_S} \frac{\sigma_{op}}{\sigma_{dc,B}}\right)^{-2} \tag{1}$$

where Z_o is the impedance of free space (377 Ω), σ_{op} is the optical conductivity, and $\sigma_{dc,B}$ is the bulk dc conductivity of the film. The term $\sigma_{op}/\sigma_{dc,B}$ is known as the conductivity ratio and is often used as a figure of merit (FoM) for the comparison of transparent conducting electrode materials.

Assuming sheet resistance to be inverse of dc conductivity with respect to thickness, the ratio terms in the equation can be simplified in terms of σ_{op} as below:

$$T = (1 + 188.5\sigma_{op}t)^{-2} \tag{2}$$

where t is the thickness of the electrode film.

However, in the case of transparent supercapacitors, the transmittance of the electrodes needs to be specified with respect to the charge storage capacity. A new capacitive figure of merit (FoMc) value is calculated from the areal-specific capacitance (C_A) and optical conductivity (σ_{op}) ratio.[39] FoMc is obtained by plotting a series of T versus C_A. The higher the FoMc values, the better the storage capacity of the electrodes at a given transmittance. It is worth noting that an electrode with ultra-high transmittance with an ultrathin material thickness will eventually result in high R_S with compromised areal capacitance (C_A). The trade-off between %T and C_A can be quantified as per eqn (3), and % T can also be obtained using eqn (2).[39,40]

$$T = \left(1 + \frac{188.5\sigma_{op}}{C_V}C_A\right)^{-2} \tag{3}$$

Furthermore, C_V/σ_{op} and C_V values can be calculated from eqn (4) and (5) below.[39,40]

$$T^{-0.5} - 1 = 188.5\frac{\sigma_{op}}{C_V}C_A \tag{4}$$

$$C_V = \text{FoMc} \times \sigma_{op} \tag{5}$$

where C_V is the volumetric capacitance (F cm^{-3}), t is the thickness and C_V/σ_{op} equals FoMc (F S^{-1} cm^{-2}).

C_A values (F cm^{-2}) are obtained using eqn (6).[41]

$$C_A = \frac{1}{A(\Delta V)v}\int_{V_1}^{V_2} I(\Delta V)dV \tag{6}$$

where A is the area of the electrode (cm^2), I is the discharge current, v is the scan rate (V s^{-1}), ΔV is the potential range between two electrodes (V), and V_1 and V_2 are the initial and end potentials of the cyclic voltammetry curve, respectively. From the galvanostatic charge–discharge profile, one can calculate the specific areal capacitance of the electrode using eqn (7).[42]

$$C_A = \frac{I\Delta t}{\Delta V} \tag{7}$$

where Δt is the discharge time in seconds (s). The energy stored in a capacitor is directly proportional to voltage squared as eqn (8).[4,42]

$$E = \frac{1}{2} \times C_A \times \frac{\Delta V^2}{3600} \tag{8}$$

where E is the areal energy density (W h cm^{-2}). Electrochemical capacitors are storage devices that can be fully charged or discharged in seconds. Thus, their power delivery or uptake of ~10 kW kg^{-1} can be achieved in seconds and is expressed as follows (eqn (9)).[4,43]

$$P = \frac{E}{\Delta t} \times 3600 \tag{9}$$

where P is the areal power density (W cm^{-2}).

Specific capacitance realized with aqueous acids is usually greater than with organic electrolytes. However, organic electrolytes are often preferred as they can offer higher operation voltage (~2.7 V) in symmetric configuration, while aqueous electrolytes provide only 1.2 V.

1.2.2. Stability. The electrode should possess excellent mechanical and electrochemical stability under different stress and chemical environments. The electrode failure leads to the loss of electrical contacts in the device, which severely reduces the performance and results in device failure. Furthermore, the electrode's metallic layer may corrode when moisture is exposed.[44,45] In addition, the dissolution of the active layer into electrolytes while charging/discharging results in ruining the performance of the electrochemical device.[46,47] Therefore, the electrodes used should warrant considerable stability for practical applications.[1]

1.2.3. Cost. Transparent conducting electrodes (TCEs) are the key components of transparent supercapacitors. ITO is the most commonly used transparent electrode for transparent electronics due to its excellent optoelectronic performance with ~90% transmittance and low sheet resistance (~10 Ω sq^{-1}). However, ITO suffers from various limitations: (1) highly expensive due to the scarcity of indium, (2) brittleness towards bending and (3) instability in acidic and alkali media, and (4) high temperature and vacuum processing due to its oxide nature.[48] As an alternative, many cost-effective TCEs have been developed using carbon materials, metal nanowires, and metal meshes during the last decade.[23] There are a few efforts in the literature to reduce the cost of alternative TCEs.[49] For example, MXene or Au grid/mesh-based TCEs are expensive, and their preparation conditions are not feasible for industrial scaling. One needs an economical and straightforward fabrication method for next-generation TCEs.

This journal is © The Royal Society of Chemistry 2023

J. Mater. Chem. A, 2023, **11**, 4907–4936 | **4909**

2. Electrode materials for transparent supercapacitors

The device with high transmittance is achieved either by reducing the active material thickness or decreasing the material loading, thus compromising the energy storage performance. Consequently, there is always a trade-off between transmittance and capacitance. There is an urge to find a cost-effective alternative to tin-doped indium oxide (ITO) as it suffers from price elevation due to increasing demand and scarcity of indium. Due to its oxide nature, the brittleness makes it implausible for adoption in futuristic large-area flexible electronics. The alternative new-generation transparent conducting materials that emerged in the last decade can be broadly classified into ultra-thin conducting materials, conducting networks, and hybrid structures, as shown in Fig. 1.

The simplest way to make transparent electrodes is by coating ultra-thin films of conducting material on a transparent substrate such as glass, polyethylene terephthalate (PET), polyethylene (PE), polydimethylsiloxane (PDMS), and polyurethane acrylate. The deciding factor for the film to be visibly transparent in the electromagnetic spectrum is maintaining the film thickness below the light absorption thickness. There are techniques developed for fabricating films that are sufficiently thin to achieve high optical transparency. However, this also increases the sheet resistance and thus deteriorates the current collection from the electrodes. This points out the trade-off between transparency, sheet resistance, and charge storage capacity. In template-based and non-template-based conducting networks, the electrodes were realized from interconnected networks prepared *via* various lithography, self-forming processes, and 1D nanomaterials. Hybrid TCEs combining two or more different electrode materials provide a promising pathway for overcoming the shortcomings of individual ones.

2.1. Ultra-thin conducting electrodes

2.1.1. Graphene. Graphene, a 2D carbon material with sp^2 hybridization in hexagonal configuration with distinctive physical properties, is the most promising alternative to silicon for flexible electronics.[50–52] High-quality graphene films are used as transparent electrodes because of their excellent optical transmittance, electrical conductance, mechanical robustness, and chemical stability. In addition, graphene is the most commonly used robust electrode material for transparent supercapacitor applications due to its large specific surface area, high transmittance, and high theoretical capacitance (550 F g^{-1}).[53] The solution processing approach with easy processability and functionalization enables the manufacturing of graphene in large quantities.[4,54] In 2010, the first report on the fabrication of a transparent supercapacitor device using vacuum-filtered graphene solution was demonstrated by Yu *et al.*[55] By adjusting the volume of the graphene solution for filtration, the thickness of the graphene layer is varied. With increasing volume, the sheet resistance (R_S) decreased with loss in transmittance. For a 25 nm thick graphene film, 135 F g^{-1} capacitance was achieved with ~70% transmittance in an aq. 2 M KCl electrolyte. The solution-processed graphene yielded high R_S due to grain boundary and structural defects and suffered from damage, cracks, and disconnected small graphene segments. In this context, graphene composites yield improved mechanical flexibility with high electrochemical performance and low R_S, for example, hybrid graphene/CNTs/Ag (Fig. 2a–c).[56] The Ag nanowires enhance the electrical conductivity of the electrode, whereas CNTs increase the interlayer spacings and thus offer many 3D open channels for the flow of electrolyte ions to enhance the capacitance. Thus, electrodes deliver ~0.31 mF cm^{-2} with 64% transmittance (Fig. 2c). While compared to bare graphene devices, a device with hybrid electrodes experiences improved flexibility.[56]
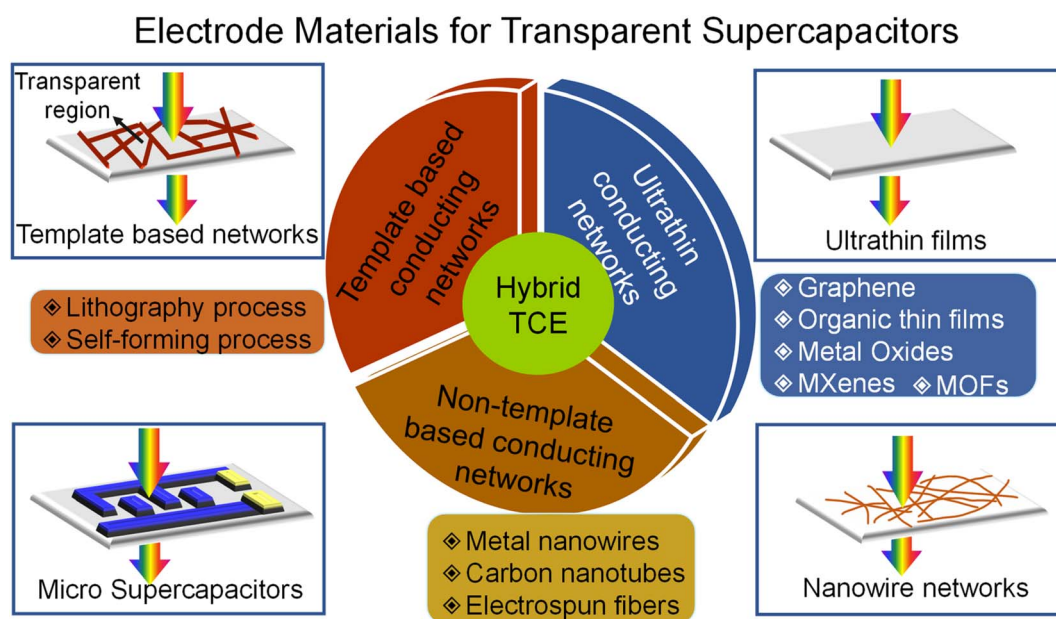

Fig. 1 Typical transparent conducting electrodes used for fabricating transparent supercapacitors.

4910 | *J. Mater. Chem. A*, 2023, **11**, 4907–4936

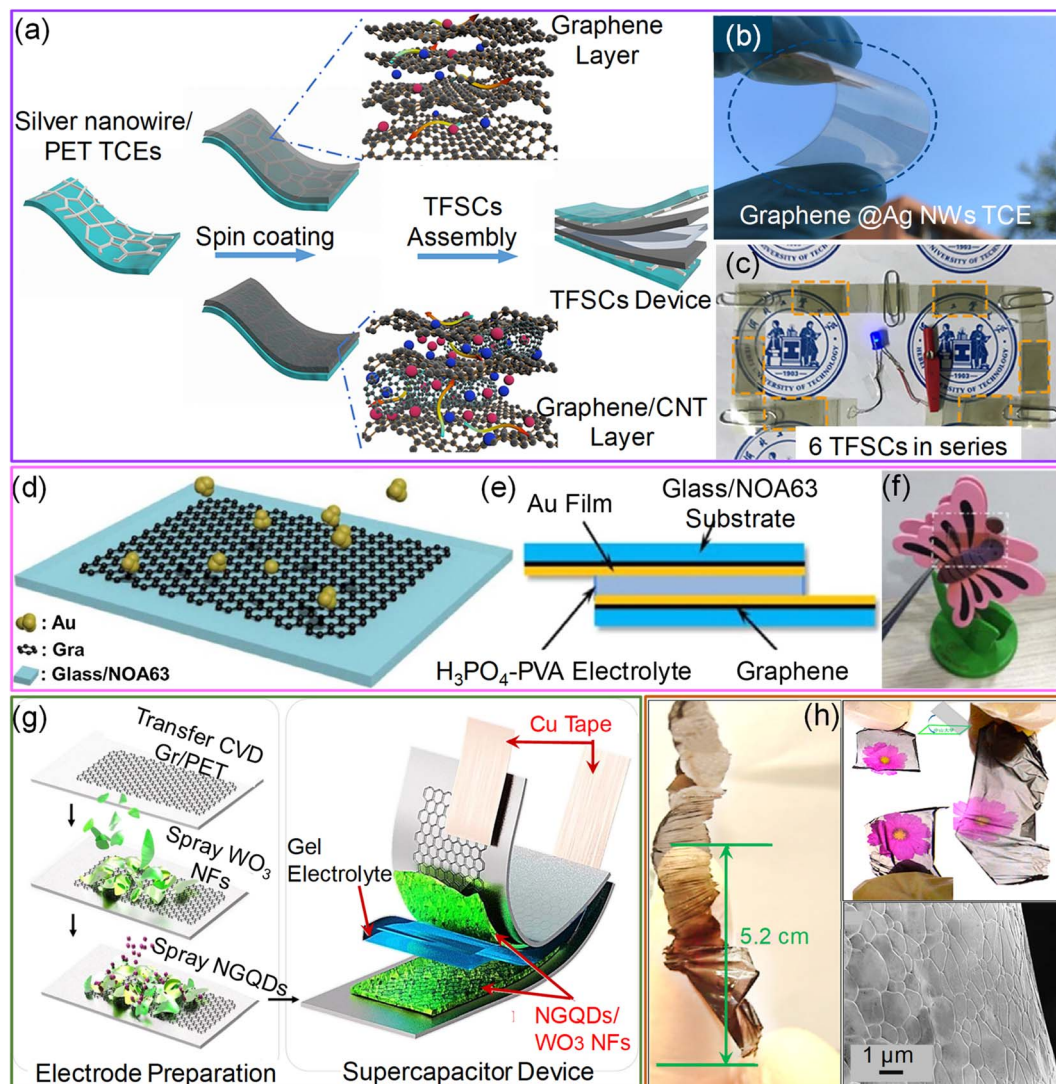This journal is © The Royal Society of Chemistry 2023

Fig. 2 Graphene: (a) schematic illustration of the fabrication of a transparent and flexible supercapacitor (TFSC) device using hybrid graphene/CNTs/Ag NWs. (b) Photographs of the prepared graphene@AgNW TCE and glowing LED by connecting six TFSCs in series (c). Reproduced with permission from ref. 56. Copyright 2018 American Chemical Society. Schematic representations of Au thin film fabrication over a graphene layer (d) and (e) supercapacitor device using a gel electrolyte. (f) Photograph of the supercapacitor device fabricated with composite materials. Reprinted with permission from ref. 61. Copyright 2019 by Elsevier. (g) Flexible and transparent supercapacitor fabricated using tungsten oxide nanoflakes, and nitrogen-doped graphene quantum dot (WO₃ NFs/NGQD) based electrodes. Reproduced with permission from ref. 62. Copyright 2020 by Elsevier. (h) Photograph of a sheet of large-area, flexible, freestanding, and transparent graphene paper (FFTGP) (left). Photographs in the upper right show FFT-GP sheets in various angles, and the lower right SEM image shows prism-like graphene microstructures of FFT-GP sheets. Reproduced with permission from ref. 42. Copyright 2015 American Chemical Society.

On the other hand, CVD-grown graphene films possess high optical transmittance and low sheet resistance with desirable robustness towards mechanical deformations. The transparent supercapacitors fabricated by sandwiching CVD-grown graphene layers (transferred to desired substrates) between electrolytes yielded a capacitance of several $\mu F\ cm^{-2}$ with high transparency.[57–60] However, the sheet resistance of monolayer graphene is several hundred $\Omega\ sq^{-1}$. The deposition of an ultrathin Au film (7 nm) over monolayer graphene brought sheet resistance down to $24.6\ \Omega\ sq^{-1}$ with a transmittance of $\sim$75% at 520 nm (Fig. 2d). An Au–graphene-based supercapacitor fabricated by sandwiching a H_3PO_4–PVA gel electrolyte yields an areal capacitance of $\sim$82 $\mu F\ cm^{-2}$, nearly 17 times higher than that of bare graphene devices (see Fig. 2e and f). A flexible supercapacitor fabricated with Au–graphene composite electrodes exhibits only 12.5% degradation even after 1800 bending cycles (bending radius, 5 mm).[61] In another example, upon CVD-grown graphene which was transferred to a PET substrate, 2D tungsten-oxide nanoflakes and 0D nitrogen-doped graphene quantum dots were deposited to develop a high-performance flexible, transparent supercapacitor (Fig. 2g). This technique is highly plausible for large-scale fabrication and patterning due to the simple synthesis methods and deposition through the spray-coating process. The

fabricated symmetric supercapacitor exhibited a specific capacitance of $\sim$180 F g^{-1} with 70% transmittance with energy and power densities of 15.8 W h kg^{-1} and 360.1 W kg^{-1}, respectively.[62]

Besides the CVD technique, graphene layers were directly grown on a SiO$_2$/Si substrate via a rapid thermal annealing (RTA) process. The advantages of the RTA process include minimal time consumption for fabrication (1–2 min) due to the rapid cooling to room temperature. They require no gas precursors, thus making them suitable for large-area fabrication. The supercapacitors fabricated by sandwiching two such graphene/PET electrodes with a PVA/H$_3$PO$_4$ gel electrolyte have shown $\sim$65% transmittance with energy and power densities of 3 W h kg^{-1} and $\sim$500 kW kg^{-1}.[63]

Making a vertically oriented 3D graphene network could be a crucial step for exploring graphene to its full potential for supercapacitor applications. Generally, efforts have focused on controlling the morphology and properties of 3D microscopic structures to obtain networks with good conductivity and large surface areas. However, for optoelectronic systems, transmittance is a crucial property to be addressed. In an example, NaCl powder was used as a template for the growth of transparent freestanding graphene paper using a microwave plasma-enhanced chemical vapor deposition (MPECVD) system (see Fig. 2h).[42] In a typical fabrication process, the carbon source was produced by decomposing CH$_4$ under high-temperature annealing (560 °C). At a microwave power of 750 W, a graphene base layer was formed on the Si substrate. NaCl powder melted entirely under a high-energy electric field and formed a thin layer over the base graphene layer. After completing the growth process, the NaCl template was etched by a physical sputtering etching process to achieve freestanding flexible and transparent graphene sheets (Fig. 2h). When employed in supercapacitor fabrication, these sheets enhanced the capacitance $\sim$1000 times compared to CVD-grown graphene supercapacitors.[42] Overall, graphene with ultrahigh transparency (>90%) and low resistance ($\sim$50 Ω sq^{-1}), and the high specific surface area for charge storage hold immense potential for transparent supercapacitor applications.

2.1.2. Organic thin films. In a flexible and transparent energy storage device, the current collecting electrode must possess excellent optoelectronic and electrochemical performance besides offering superior flexibility.[48] The most widely used indium tin oxide (ITO) exhibits excellent optoelectronic properties, but its brittle nature remains a great constraint for its use in flexible electronics. In this context, conducting polymers like poly(3,4-ethylene dioxythiophene):(styrene sulphonate) (PEDOT:PSS) and polypyrrole (PPy) exhibit various advantages like high transmittance with low sheet resistance and superior electrochemical performance with high flexibility.[64,65]

2.1.2.1. PEDOT:PSS. The usage of PEDOT as an electrode material in electrochemical capacitors dates back to 1997. The addition of PSS enhances the conductivity of PEDOT and thus helps in improving capacitance.[66,67] For instance, PEDOT:PSS electrodes sandwiched with H$_3$PO$_4$/PVA gel electrolytes result in high-performance transparent all-solid-state supercapacitors

with an areal (gravimetric) capacitance of $\sim$4.72 mF cm^{-2} (27.76 F g^{-1}). With increasing PEDOT:PSS layer thickness, the specific capacitance increased drastically with an increase in the mass of the active materials (PEDOT), whereas the transmittance of the device decreased to $\sim$55% at 550 nm. The maximum power and energy densities of 0.036 W cm^{-2} and 0.38 mW h cm^{-2} were achieved.[68] Besides PSS, secondary dopants like sorbitol, H$_2$SO$_4$, dimethyl sulfoxide, methanol, and ethylene glycol dramatically increase the electrical conductivity.[25] In another report, the conductivity of the PEDOT:PSS layer was enhanced by dipping the films in formic acid (FA) for just a few seconds at room temperature.[25] There was an exponential decrease in sheet resistance by three orders of magnitude from 1.5×10^5 Ω sq^{-1} to 10^2 Ω sq^{-1}. The FoM value (σ_{dc}/σ_{op}) of the PEDOT:PSS films dipped in FA is 39, much higher than that of SWCNT-based electrodes. PEDOT: PSS films doped with FA have shown excellent electrochemical performance with an areal capacitance (C_A) of 1.9 mF cm^{-2} and 0.18 mF cm^{-2} for 70% and 99% transparent films, respectively.[25] Further enhancement in the capacitance of PEDOT:PSS electrodes was forbidden by their intrinsic optoelectronic properties (R_S > 100 Ω sq^{-1}).

In this respect, hybrid electrodes are ideal for reducing the R_S to below 10 Ω sq^{-1}. The hybrid electrodes composed of metal nanowires, grids, fibers, and nano- and micro-meshes with PEDOT:PSS improve the electrochemical performance due to the highly conducting metal backbone structures. For instance, embedded AgNWs/PEDOT:PSS electrodes with a novel interlayer composed of Ni(OH)$_2$ and polyethyleneimine ethoxylated (PEIE) yield a remarkable volumetric capacitance of 443 F cm^{-3} with 86% transparency. In addition, the bifunctional electrochromic supercapacitor device fabricated using this hybrid electrode shows a fast-switching speed with cycle stability of 10 000 charge–discharge cycles. The main reason for such enhancement in capacitance is the improved pore density of PEDOT:PSS with the Ni(OH)$_2$–PEIE interlayer.[69] Later, an ultra-smooth embedded PEDOT:PSS/AgNFs/NOA-63 hybrid electrode was fabricated by sandwiching free-standing Ag nanofibers with a PEDOT:PSS film and photopolymer Norland Optical Adhesive, NOA 63. The resulting electrode exhibited high transmittance (85%), low sheet resistance ($\sim$2.1 Ω sq^{-1}), and excellent mechanical stability. The transparent supercapacitor device fabricated with a hybrid electrode possesses excellent electrochemical performance (3.64 mF cm^{-2}) and mechanical flexibility (Fig. 3a–c).[70]

2.1.2.2. Polypyrrole. Due to its high storage capacity, environmental stability, and cost-effective fabrication, polypyrrole (PPy) has been used as an active material for supercapacitors since 1960.[71–73] A simple, cost-effective solution-processing interfacial chemical oxidative polymerization method is highly considered for large-area fabrication.[74,75] In this process, the polymerization time controls the prepared film's thickness, haze, and conductivity. For example, Jiao et al. synthesized a PPy/PET film with the dimensions of 25 × 15 cm^2 with good transparency (71%), low haze (1.4%) and sheet resistance (0.78 kΩ sq^{-1}) (see Fig. 4a).[40] In the preparation process, a PET film was floated on the surface of a solution containing iron chloride and 2,6-naphthalene disulfonic acid disodium dissolved in an
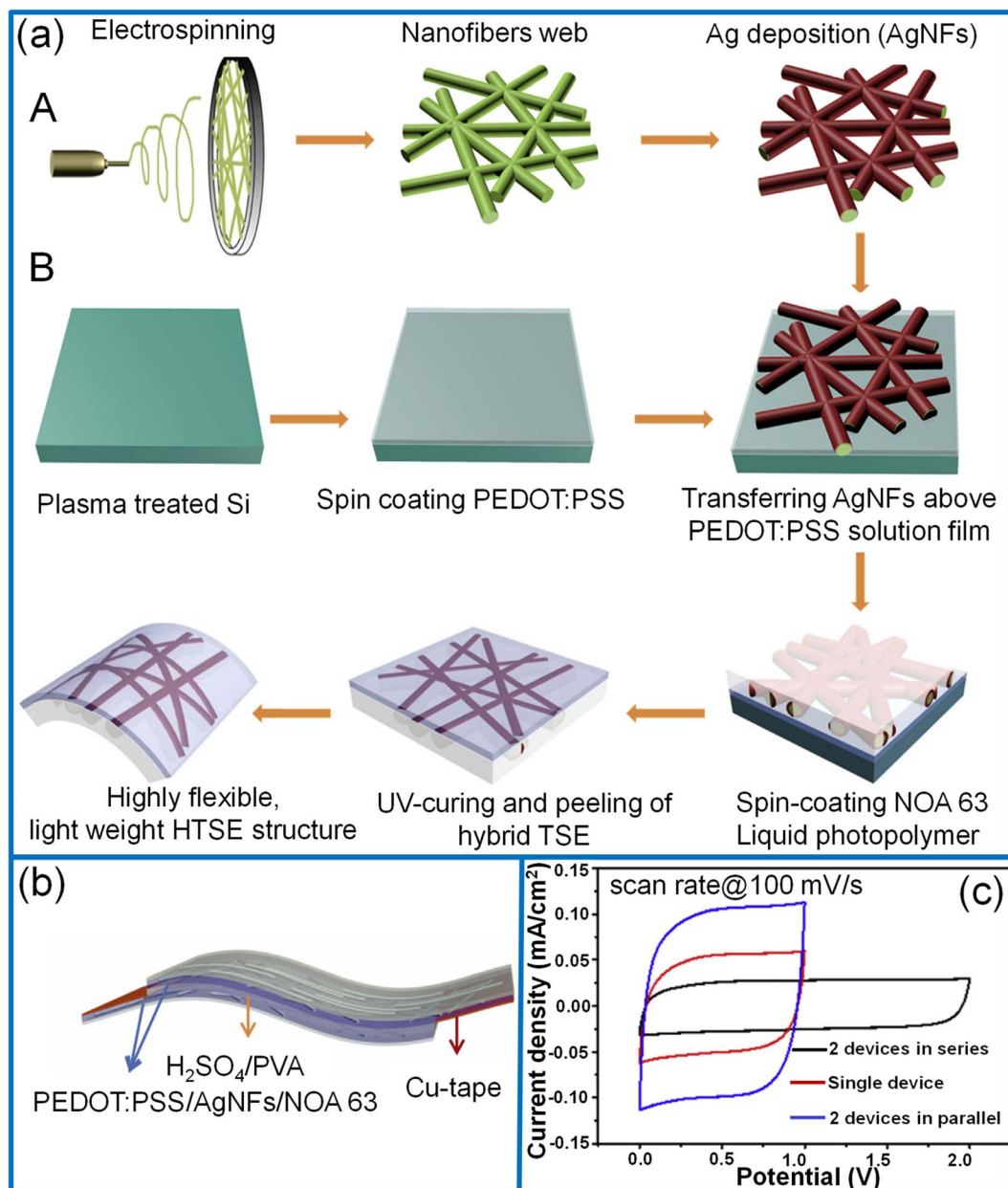
4912 | *J. Mater. Chem. A*, 2023, **11**, 4907–4936

This journal is © The Royal Society of Chemistry 2023

Fig. 3 PEDOT:PSS: (a) schematic illustration of the fabrication of the PEDOT:PSS/Ag nanofibers/NOA 63 hybrid transparent supercapacitor electrode (HTSE) structure. (b) Schematic diagram of the transparent solid-state supercapacitor device fabricated by assembling two HTSEs with a gel electrolyte in between. (c) Cyclic voltammogram curves of a single solid-state supercapacitor device compared with two devices connected in series and parallel configurations at a scan rate of 100 mV s^{-1}. Reprinted with permission from ref. 70. Copyright 2019 by Elsevier.

organic solvent and water mixture which was maintained at ~4 °C. The pyrrole monomer dissolved in a similar organic solvent/water mixture was slowly added to the above mixture solution to initiate the polymerization in the interfacial region between PET and the liquid. During the polymerization process, a thin layer of PPy was deposited on the lower surface of the PET film. After the desired deposition time, the PPy/PET film was taken out, rinsed, and dried to obtain the TCE. During the synthesis, the organic solvent added in a small volume enhances the solubility of the pyrrole monomer and induces homogeneous polymerization on the surface of the PET. In

order to make PET float on the liquid surface, the optimum ratio of methanol and water (1 : 9) was taken as the PET surface is hydrophobic and organic solvents wet the PET surface more easily and help in easier absorption of PPy monomers on the PET surface. It is also noticed that the mole ratio of pyrrole and iron chloride (FeCl$_3$) must be maintained above one for the uniform and continuous formation of the PPy film. Compared to electrochemical oxidation, this method is highly facile, less time-consuming, and cost-effective. The electrochemical performance of the symmetric sandwich-structured supercapacitor was demonstrated by assembling two PPy electrodes
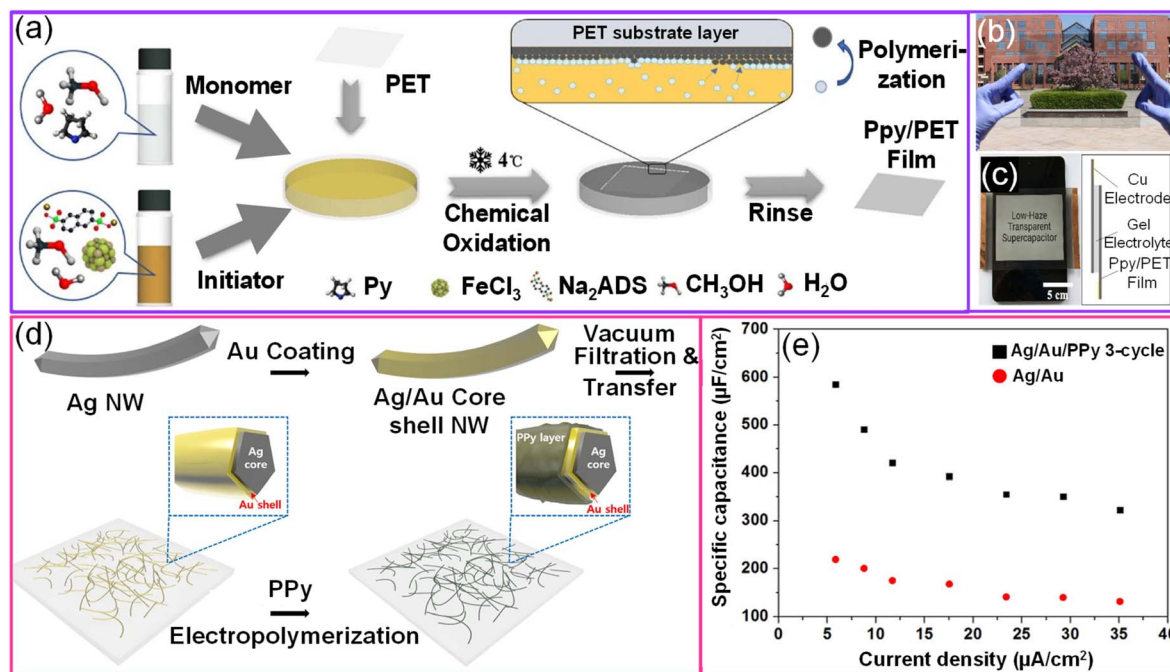
Fig. 4 Polypyrrole: (a) schematic representation of fabrication of PPy/PET-based transparent conducting low-haze electrodes through an interfacial polymerization technique. (b) Photograph of a large-area TCE (17×22 cm^2) and a fabricated large-area supercapacitor (c). Reprinted with permission from ref. 40. Copyright 2018 American Chemical Society. (d) Schematic representation of fabrication steps for Ag/Au/PPy electrodes. (e) The dependence of the specific areal capacitance of bare Ag/Au NWs and Ag/Au/PPy NWs on the discharging current densities. Adapted with permission from ref. 76. Copyright 2017 by Springer Nature.

with a H$_3$PO$_4$/PVA gel electrolyte. The fabricated large-area supercapacitor (20×15 cm^2) exhibited low haze (1.54%) with nearly 47% transmittance at 550 nm with a specific areal capacitance of 1.45 mF cm^{-2} (Fig. 4b and c).[40] Using a strategy of DMF etchant-writing, the desired interdigital channel pattern for the micro-supercapacitors was obtained on the PET substrate. The fabricated micro-supercapacitor showed ∼70% transmittance and yielded areal capacitance, energy, and power densities of 1.64 mF cm^{-2}, 5 mW h cm^{-3}, and 67.3 mW cm^{-3}, respectively.[40] Direct electro-polymerization onto the transparent current collector is another more promising way of fabrication. Moon *et al.* first reported an Ag/Au/PPy flexible transparent electrode by direct electro-polymerization of PPy over a conducting network (Fig. 4d).[76] The thickness of the PPy coating over the nanowire network was determined by sweep cycles at 0.2 V s^{-1} in the voltage range from 0 to 1.0 V. With an increasing number of deposition cycles (20), the diameter of Ag/Au/PPy nanowires increased to 136 nm with 62% transmittance. The nanowires with three sweep cycles exhibited high opto-electronic performance (∼85% transmittance) and capacitance (Fig. 4e). In addition, the fabricated flexible symmetric super-capacitor had a negligible capacitance loss while bending (bending radius, 5–30 mm).[76]

2.1.3. Metal oxides

2.1.3.1. Tin-doped indium oxide (ITO). Transparent conducting metal oxide coatings are commonly used as a current collector for transparent supercapacitors. For instance, transparent, flexible, and solid-state supercapacitors have been

fabricated on ITO using room-temperature ionic liquid (RTIL) gel. The RTIL gel composed of 1-butyl-3-methylimidazolium chloride ([BMIM][Cl]) and 6 wt% cellulose nanoparticles forms a transparent electrolyte after drying. ITO is deposited on a polyethylene naphthalate (PEN) substrate through high target utilization sputtering (HiTUS) technology that yields a smooth surface. The average ITO thickness on the PEN substrate is ∼470 nm with 92% transmittance (between 450 nm and 800 nm) and 7.7 Ω sq^{-1} sheet resistance. The specific capacitance calculated from galvanostatic charge–discharge measurements of ITO/[BMIM][Cl]/ITO is ∼18 F g^{-1}. This is the first EDLC-type supercapacitor based on an ionic liquid gel.[77] The deposition of transition metal oxides like Co$_3$O$_4$, MnO$_2$, and RuO$_2$ enhances the capacitance and cycling life compared to bare ITO electrodes due to high electrochemical performance. Liu *et al.* have coated Co$_3$O$_4$ nanocrystals synthesized *via* a laser ablation in liquid (LAL) technique on an ITO/PET (15 Ω sq^{-1}) substrate and fabricated a solid-state supercapacitor by assembling two such electrodes with a PVA/H$_3$PO$_4$ gel electrolyte. The cyclic voltam-mogram curves with two strong redox peaks indicate the pseudocapacitive nature of the supercapacitor. The super-capacitor delivers a specific capacitance of 172 F g^{-1} and an areal capacitance of 6.03 mF cm^{-2} with maximum energy and power densities of 3.01 W h kg^{-1} and 1.152 kW kg^{-1}. The fabricated supercapacitor is 51% transparent at a wavelength of 550 nm. It is worth noting that even after 20 000 cycles, the capacitance retention is 100% which decreased to 93% after 30 000 cycles. The main factors contributing to excellent cycling

4914 | *J. Mater. Chem. A*, 2023, **11**, 4907–4936

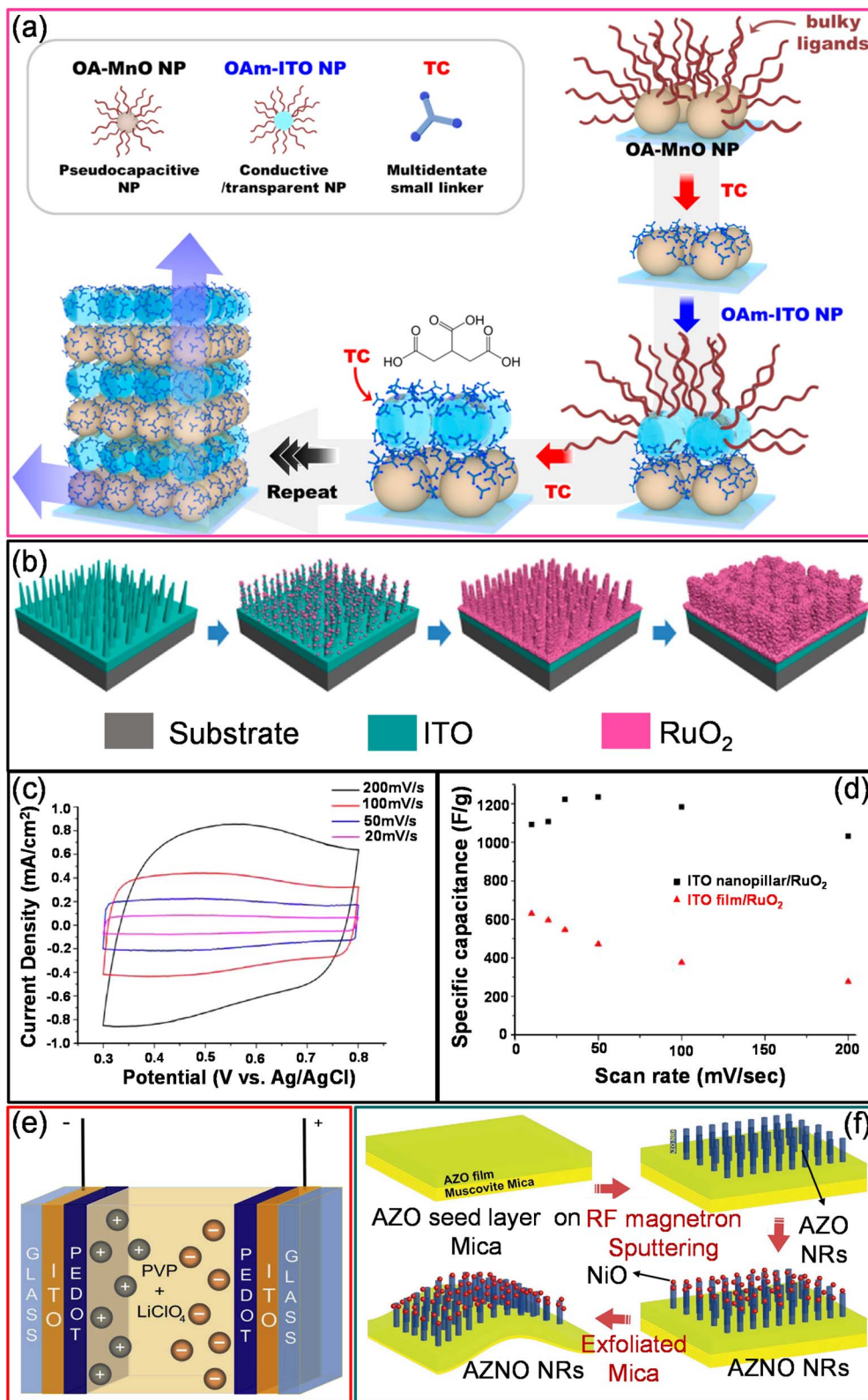This journal is © The Royal Society of Chemistry 2023

Fig. 5 Metal oxides: (a) schematic diagram of the formation of a MnO NP-based flexible solid-state transparent supercapacitor (TSC) with ITO NPs. Reproduced with permission from ref. 81. Copyright 2020 American Chemical Society. (b) Schematic representation of fabrication of the coaxial ITO and RuO_2-based core–shell electrode. (c) CV curves of ITO nanopillars coated with RuO_2 (30 cycles) at various scan rates. (d) Comparison of the specific capacitance of bare ITO nanopillars and RuO_2-coated ITO nanopillars at various scan rates. Reproduced with permission from ref. 82. Copyright 2014 American Chemical Society. (e) Schematic diagram illustrating the electrode configuration of a transparent supercapacitor with ITO/PEDOT-based electrodes. Reprinted with permission from ref. 83. Copyright 2013 by Elsevier. (f) Schematic illustrations of the AZO nanorod and AZO/NiO nanorod heterostructure fabrication process using RF magnetron sputtering on a muscovite substrate. Reproduced with permission from ref. 85. Copyright 2020 by John Wiley and Sons.

This journal is © The Royal Society of Chemistry 2023

J. Mater. Chem. A, 2023, 11, 4907–4936 | 4915

stability are the high surface-to-volume ratio and the clean surface (devoid of contaminants) of Co_3O_4 nanocrystals.[78] Similarly, MnO_2 thin films were electrochemically deposited onto an ITO/PET substrate due to their high theoretical specific capacitance, low cost, and eco-friendly properties. The transparent symmetrical supercapacitor device with two ITO/MnO_2 electrodes sandwiched with a K_2SO_4/SiO_2 composite gel electrolyte exhibit a capacitance of 15 mF cm^{-2}.[79] The MnO_2 thin-film electrodes have also been directly grown on ITO/PET using a facile and inexpensive chemical bath deposition technique. The MnO_2 thin film offers a specular transmittance of 77.4% at 550 nm. The ITO/MnO_2 thin-film electrodes exhibited a specific capacitance and areal capacitance of ~230 F g^{-1} and 9.2 mF cm^{-2} in a 1 M Na_2SO_4 electrolyte.[80] As an alternative, ligand-mediated layer-by-layer (LbL) assembly is another simple process that utilizes complementary interactions between the molecules to prepare ultrathin composite films with the desired thickness, compositions, and functionalities. High-energy pseudocapacitive (OA–MnO) nanoparticles and conducting oxide (OAm–ITO) nanoparticles were LbL-assembled using a ligand exchange between native ligands (oleic acid (OA)/oleylamine (OAm)) and tricarballylic acid (TC), a small multidentate linker (Fig. 5a).[81] The introduced TC linker substantially reduced the inter-distance between the adjacent NPs, thereby reducing the resistance of the electrodes. Additionally, the periodic deposition of ITO NPs and MnO NPs significantly enhances the areal capacitance by reducing the charge transfer resistance without substantial transmittance loss. The electrochemical storage capability of (MnO NP/TC/ITO NP/TC)$_{50}$ electrodes was investigated in a 0.5 M Na_2SO_4 electrolyte. After the deposition of ITO NPs, the areal capacitance of the device increased to 40.5 mF cm^{-2} (T%, 60.8%) from the initial value of 24.6 mF cm^{-2} (T%, 61.6) with no ITO NPs.[81] In another example, standing ITO nanopillars ($T \sim 64\%$) fabricated using a radio-frequency (RF) sputtering technique have been used as a current collector instead of ITO films (Fig. 5b). The electrochemical deposition of pseudocapacitive materials like RuO_2 on ITO nanopillars enhances the specific capacitance (1235 F g^{-1}) due to facilitated charge transfer and ion diffusion across standing coaxial nanostructures (Fig. 5c and d).[82]

On the other hand, ITO-based heterogeneous film supercapacitors fabricated with CNTs and PEDOT exhibit high specific capacitance. Instead of bare ITO, ITO/PEDOT electrodes have also been utilized. By sandwiching two ITO/PEDOT electrodes with PVP/LiClO$_4$ solid polymer electrolyte films, a supercapacitor with a maximum transmittance of ~50% between 370 and 770 nm with a maximum specific capacitance of 15 F g^{-1} is obtained (Fig. 5e).[83] Chen *et al.* realized transparent supercapacitors with 30 wt% In_2O_3 nanowires and CNT composites. The device offers ~50% transmittance with energy and power densities of 1.29 W h kg^{-1} and 7.48 kW kg^{-1}, respectively.[84]

2.1.3.2. Aluminum-doped zinc oxide (AZO). AZO is another commonly used transparent conducting material for commercial applications mainly due to its excellent electrical and optical properties, low cost, and non-toxicity. Furthermore, oxides with 1D nanostructures like nanowires, nanorods, nanofibers, *etc.*, are of great interest due to their high surface

area with short carrier diffusion lengths. Le *et al.* have prepared flexible and transparent AZO nanorods and AZO/NiO nanorods on mica through radio-frequency (RF) sputtering.[85] Its potential for energy storage applications was explored by sandwiching two AZO/NiO nanorod electrodes with a PVA/KOH gel electrolyte, as shown in Fig. 5f. The specific capacitance calculated from the galvanostatic charge–discharge curve is 3.4 mF cm^{-2} with 80% transmittance. The energy and power densities of the device are 45.38 nW h cm^{-2} and 4.97 μW h cm^{-2}, respectively.[85]

2.1.3.3. Molybdenum trioxide (MoO_3). An ultralong molybdenum trioxide nanobelts with an average length of 200 μm with a length-to-width ratio of almost 1000 were synthesized using the hydrothermal technique. The reaction completion was evident from the change in the color of orange peroxomolybdic acid into a white suspension of MoO_3 nanobelts. The prepared nanobelts remained well dispersed in ethanol without aggregation, even for a year. The formed nanobelts are shown to be thermochemically stable up to 788 °C. Freestanding transparent and mechanically flexible yet robust MoO_3 nanopaper with a thickness of several hundred nanometers was prepared by simple vacuum filtration of MoO_3 nanobelt suspension and the subsequent peeling-off process. The transparent nanopaper is a 3D network of MoO_3 nanobelts with large pores in-between nanobelts. These pores highly facilitate ion diffusion in freestanding 3D networks. The nanopaper with 0.076 mg cm^{-2} offers ~90% transmittance. The symmetric supercapacitor device with two MoO_3 nanopaper assembled with a 5 M LiCl or PVA/LiCl gel electrolyte exhibits a specific capacitance of ~258 F g^{-1}, which slowly decreased to ~95 F g^{-1} for a scan rate of 200 mV s^{-1}. The device exhibits 96.5% capacitance retention even after 20 000 cycles of charge–discharge. The device's maximum energy and power densities were 22.89 W h kg^{-1} and 10.1 kW kg^{-1}, respectively.[86]

2.1.4. MXenes. Since their discovery (2011), MXenes have found applications in many thriving areas.[87,88] Due to surface functional groups, MXenes possess a hydrophilic nature and form a stable aqueous solution that can be used to form composites and for device fabrication.[89,90] In addition, titanium carbide MXenes ($Ti_3C_2T_x$) exhibit high metallic conductivity (9880 S cm^{-1}).[39] Monolayer/few-layer MXene nanosheets are optically transparent and possess excellent electronic conductivity and fast faradaic reactions (pseudocapacitance). The pioneering work on TCE fabrication using Ti_3AlC_2 was done by Halim *et al.* through simple sputter deposition followed by Al selective etching.[90] A 19 nm thick film exhibits ~90% transmittance in the visible region. However, deposition at a higher temperature (900 °C) and metal (Al) etching remains a greater limitation for upscaling. Gogotsi *et al.* adopted a simple spray coating technique and prepared a TCE with transmittance ranging from 40% to 91% for films with 5 to 70 nm thickness.[91] At $t = 70$ nm ($T = 40\%$), the sheet resistance of the film is 500 Ω sq^{-1}, which increased to 8 kΩ sq^{-1} when the film thickness was reduced to 5 nm. While spray coating, the MXene droplets are purged with gas and are deposited over the hot substrate (see Fig. 6a). The vapor bubbles create plenty of nano/micropores during the solvent (water/ethanol) evaporation from the substrates, hindering smooth charge transport across the
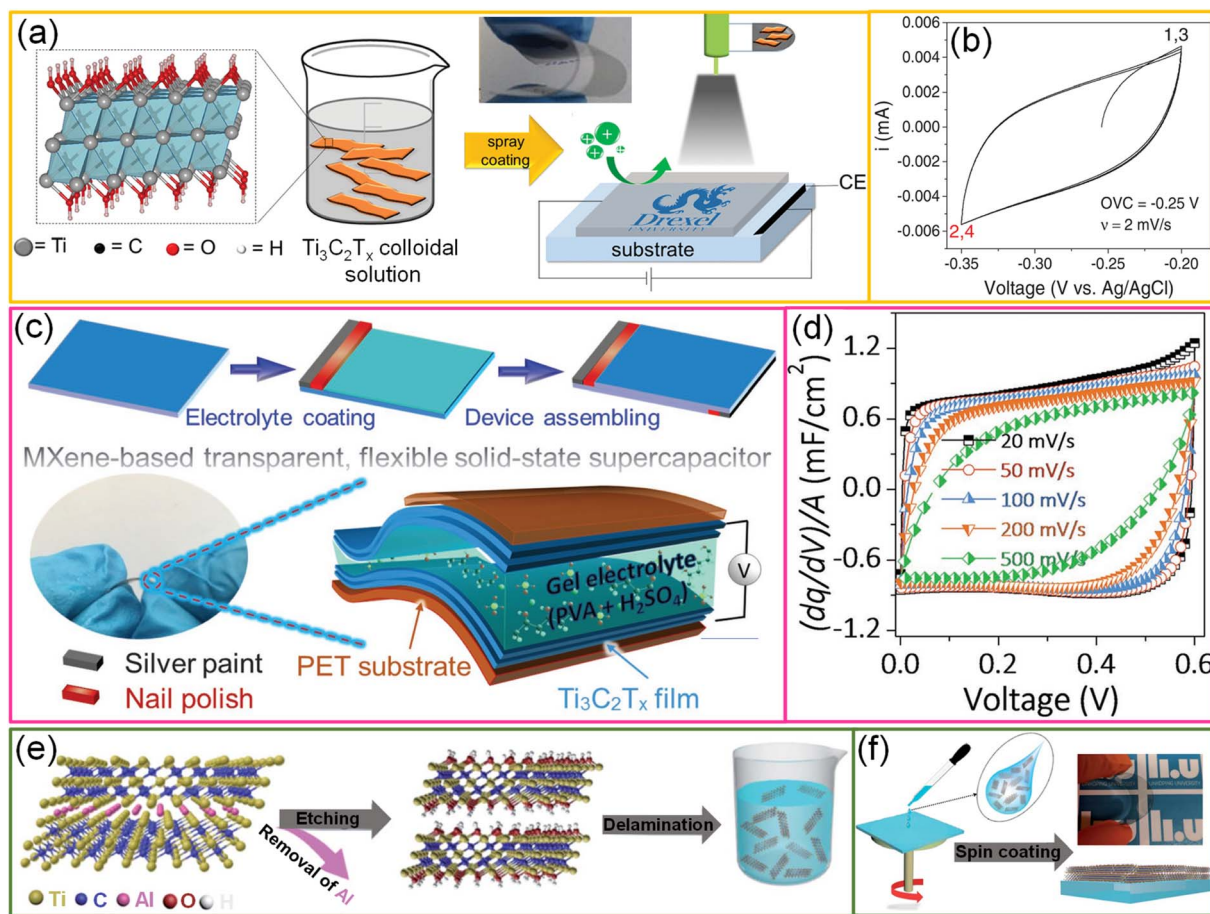
4916 | *J. Mater. Chem. A*, 2023, **11**, 4907–4936

This journal is © The Royal Society of Chemistry 2023

Fig. 6 MXenes: (a) schematic representation of fabrication of a $Ti_3C_2T_x$ thin film through the spray coating process. The structure of $Ti_3C_2T_x$ is given in the box where Ti, O, H and C represent gray, red, white, and black, respectively. Inset shows the high degree of flexibility of the $Ti_3C_2T_x$ thin film. (b) CV curve of the $Ti_3C_2T_x$ MXene thin film in a 3-electrode configuration. Reproduced with permission from ref. 91. Copyright 2016 by John Wiley and Sons. (c) Schematic representing the fabrication of a $Ti_3C_2T_x$ MXene-based flexible solid-state transparent supercapacitor device and its corresponding cyclic voltammogram curves are given in (d). Reproduced with permission from ref. 39. Copyright 2017 by John Wiley and Sons. (e) Schematic depiction of preparation of the Ti_3AlC_2 precursor using a minimally intensive layer delamination (MILD) process. (f) Schematic illustration of the preparation of a MXene-based transparent electrode via a spin coating approach. Reproduced from ref. 92 with permission from the Royal Society of Chemistry.

stacked random network. The electrochemical properties of the prepared MXenes were further examined in a typical three-electrode configuration, and the capacitance nature was further from their rectangular CV curves, especially in the narrow voltage window from −0.2 to −0.35 V (Fig. 6b).[91]

To explore the performance of all MXene-based supercapacitor devices, two $Ti_3C_2T_x$ TCEs (91%, T) are sandwiched with a gel electrolyte, and the fabricated symmetric supercapacitor devices have shown ∼80% transmittance (Fig. 6c).[39] The capacitive nature of the device is evidenced by its linear galvanostatic charge–discharge curves, rectangular shapes of cyclic voltammograms, and quick current response upon voltage reversal (Fig. 6d). The areal capacitance of the symmetric device is 0.86 mF cm^{-2}. The asymmetric device was fabricated by sandwiching SWCNTs and $Ti_3C_2T_x$ TCEs in sequence. Due to the broader voltage window offered in an asymmetric configuration, the energy and power densities of the device were enhanced to 0.05 μW h cm^{-2} and 2.4 μW cm^{-2},

respectively.[39] In another example, Qin et al. fabricated $Ti_3C_2T_x$ MXene-based flexible, semitransparent solid-state photovoltaic supercapacitors (PSCs) through the vertical stacking method.[92] The $Ti_3C_2T_x$ film aligned parallel to the substrate while spin coating, demonstrating outstanding conductivity, flexibility, and transmittance (Fig. 6e and f). These properties make the MXene film an efficient TCE for OPVs with a high photo-conversion efficiency of 13.6% and an active material for supercapacitors resulting in a high volumetric capacitance of 502 F cm^{-3} with a high average transmittance of 33.5%. In addition, the usage of organic solid ion gel electrolytes compared to water-based electrolytes increases the cycling stability of the device.[92] Although MXene-based devices exhibit excellent charge-storage capability and optoelectronic properties, the instability of MXene dispersions and devices in the ambient environment is the bottleneck. However, the shelf-life of MXene-based dispersions is extended by proper storage. Besides the stability, the high cost of Ti_3AlC_2 MAX (∼$550/150 g)

is the other biggest challenge hindering MXene-based products from entering the market.[37]

2.1.5. Metal–organic frameworks (MOFs). Metal–organic frameworks (MOF) are crystalline but porous materials prepared through coordination between organic linkers and metal clusters/sites.[93] MOFs offer a large specific surface area (7000 m^2 g^{-1}), enhancing the capacitance due to the orderly arrangement of pores. $Ni_3(HITP)_2$ (HITP = 2,3,6,7,10,11-hexaminotriphenylene) MOFs are an active material for fabricating transparent supercapacitors due to their excellent conductivity with tunable transmittance.[94] Dinca and coworkers pioneered the synthesis of $Ni_3(HITP)_2$ MOFs through coordination interactions between Ni ions and HITP ligands.[94] These MOFs possess 2D hexagonal lattice structures. $Ni_3(HITP)_2$ films were synthesized through a modified air/liquid interfacial method and controlled the film thickness linearly with the reaction time (see Fig. 7a).[95] The MOF film prepared with a 30 minute reaction duration ($Ni_3(HITP)_2$-30) offers optimal transmittance (78.4%) and sheet resistance (51.3 Ω sq^{-1}) with an average thickness of 20 nm (Fig. 7b).[95] The prepared films have a highly uniform and continuous morphology with low surface roughness ($\sim$2 nm).

The electrochemical performance of the $Ni_3(HITP)_2$-30 thin film was evaluated in a potential window of -0.1 to 0.4 V at various scan rates (1 to 5000 mV s^{-1}). The ideal capacitive nature of the device was evidenced by its rectangular cyclic voltammogram curves and triangular charge–discharge profiles without any voltage drops. An areal capacitance of 1.63 mF cm^{-2} was achieved at a current density of 5 μA cm^{-2}. This increment in capacitance values is mainly due to the efficient penetration and fast ion diffusion effect of the MOF electrodes. An all-solid-state flexible transparent (55.8%) supercapacitor was fabricated by overlaying two MOF electrodes with a PVA/KCl hydrogel as the electrolyte and separator. An areal capacitance of 1.35 mF cm^{-2} was achieved at a current density of 10 μA cm^{-2} (Fig. 7c).[95] Furthermore, with an asymmetric supercapacitor ($Ni_3(HITP)_2$‖PEDOT:PSS), an areal capacitance of 1.06 mF cm^{-2} was achieved at 3 μA cm^{-2}. This $Ni_3(HITP)_2$ based supercapacitor device exhibits a remarkable capability of up to 5000 mV s^{-1}.[95]

2.2. Conducting networks

Unlike thin film conducting electrodes, network structures have designated conducting paths while the remaining regions
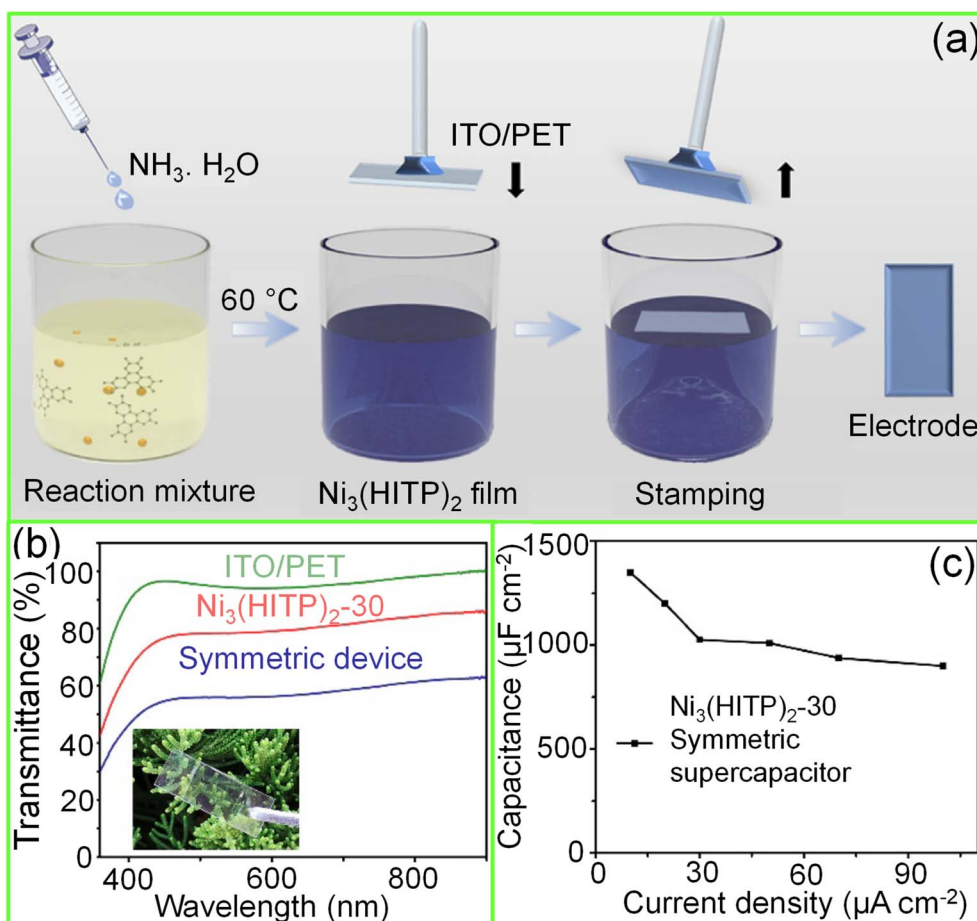
Fig. 7 Metal–organic frameworks (MOFs): (a) schematic illustration of the fabrication of a $Ni_3(HITP)_2$ thin film over an ITO/PET substrate using the Langmuir–Schäfer method. (b) The transmittance spectra of the symmetric supercapacitor device compared with ITO/PET and $Ni_3(HITP)_2$-30 electrodes. Inset shows the photograph of the device. (c) The areal capacitance of the device plotted *versus* different current densities. Reprinted with permission from ref. 95. Copyright 2020 by Elsevier.

4918 | *J. Mater. Chem. A*, 2023, **11**, 4907–4936

This journal is © The Royal Society of Chemistry 2023

transmit the incident light. Conducting network-based TCEs are broadly classified into non-template-based networks and template-based networks. The TCEs fabricated using a non-template-based approach are usually formed by brute force and therefore experience random conducting paths and cross-bar junctions. The electrical conductivity mainly occurs due to the percolative paths. In contrast, template-based networks are fabricated *via* the lithography approach, and thus the network remains in a plane without cross-bar junctions. However,
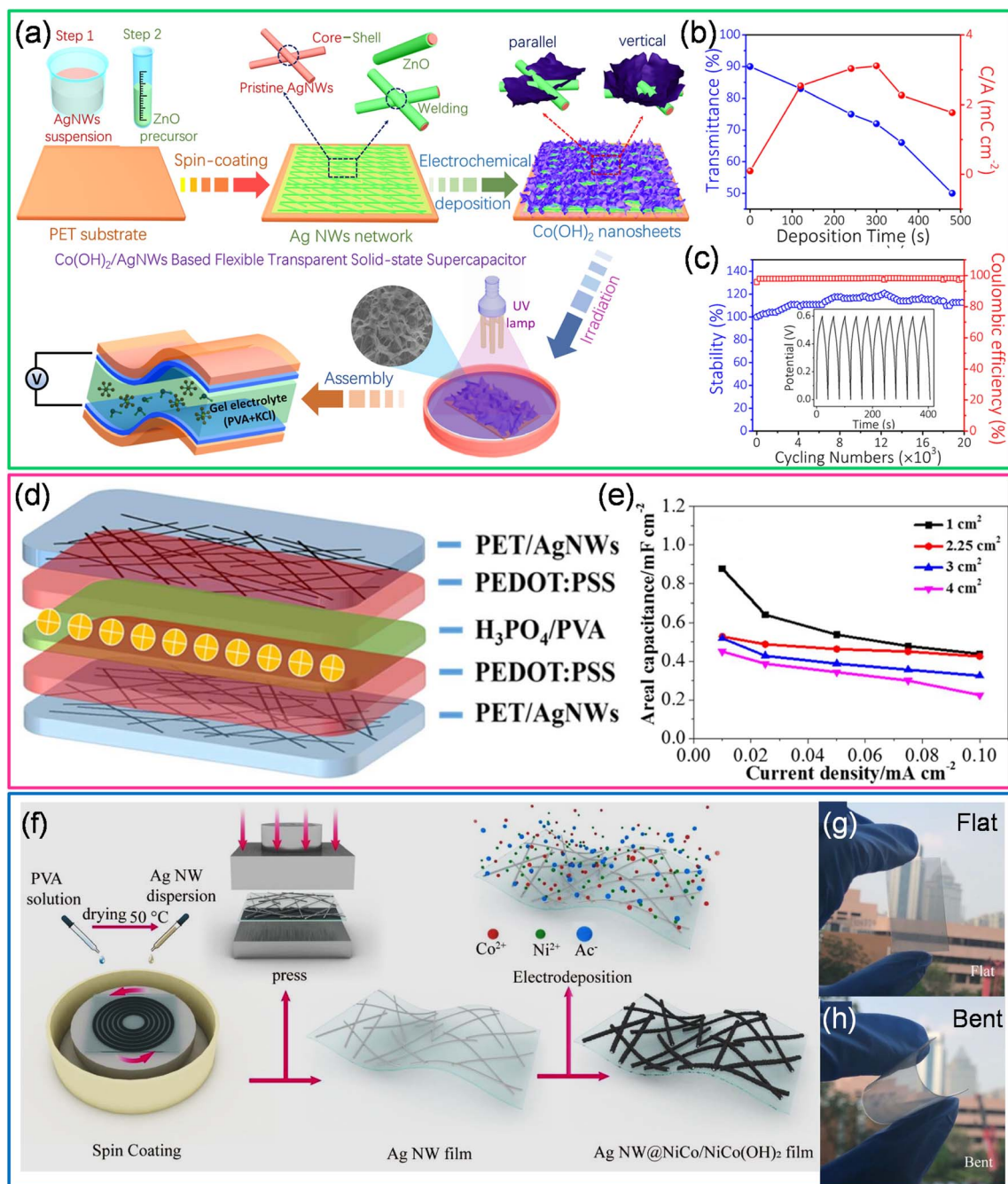

Fig. 8 Metal nanowires: (a) schematic illustration of the fabrication of a transparent supercapacitor based on a Co(OH)$_2$ nanosheets/Ag nanowire hybrid network. (b) The variation in optical transmittance and C/A with change in Co(OH)$_2$ deposition times. (c) The stability and coulombic efficiency of the device *versus* the number of charge–discharge cycles. Reprinted with permission from ref. 97. Copyright 2019 American Chemical Society. (d) Schematic illustration of the fabrication of an all solid-state flexible supercapacitor with Ag NWs and PEDOT:PSS. (e) The areal capacitance was calculated from galvanostatic charge–discharge profiles for supercapacitors with various device areas. Reproduced with permission from ref. 98. Copyright 2018 American Chemical Society. (f) Schematic representation of fabrication of Ag NW@NiCo/NiCo(OH)$_2$ electrodes. (g) and (h) Photographs of the electrode in flat and bent positions. Reproduced from ref. 99 with permission from the Royal Society of Chemistry.

template-based networks sometimes suffer from diffraction effects due to the orderliness of the network patterns.[51]

2.2.1. Non-template based networks

2.2.1.1. Metal nanowires. Achieving high transmittance and conductance with excellent stretchability in a capacitance device is extremely difficult, especially with thin conducting films, as there is a tradeoff between film thickness and conductivity. In the case of metal nanowires, by controlling the volume of nanowires and increasing the aspect ratio of nanowires, there is an improvement in the device's conductivity and transparency. Nanowire networks are sparely interconnected below a critical density (percolation threshold), and above this, the network conductivity increases drastically with an increase in the density of the nanowires. Therefore, conduction in metal nanowires is best described by percolation theory.[49]

Gong *et al.* fabricated a transparent supercapacitor using ultrathin gold nanowires (AuNWs), which are soft and serpentine-like at the nanoscale due to their ultrathin (diameter, 2 nm) and ultralong morphology (aspect ratio, >10 000).[96] Ultrathin AuNWs were synthesized by adding oleylamine (OA, 1.5 mL) to gold salt ($HAuCl_4 \cdot 3H_2O$, 44 mg) in hexane (40 mL). The OA acts as a phase transfer reagent and helps in the complete dissolution of gold salt. After adding triisopropylsilane (TIPS, 2 mL), the solution was left to stand (2 days) without stirring until the solution changed from its initial yellow color to dark red, indicating the formation of AuNWs. The monolayer of AuNWs was achieved through a modified Langmuir–Blodgett technique. The AuNW-based all-solid-state (PVA/KNO_3) transparent supercapacitor (79%) shows excellent stability towards stretching (up to 30%) due to its aligned wavy structures. The supercapacitor showed an areal specific capacitance of 226.8 μF cm^{-2} and a specific capacitance of 8.5 F g^{-1}.[96]

In another example, AgNWs coated with vertically aligned $Co(OH)_2$ are employed for supercapacitor fabrication as 2D-$Co(OH)_2$ possesses high interlayer spacings and high theoretical capacitance (3460 F g^{-1}) and low cost (see Fig. 8a).[97] AgNW suspension was spin-coated on a PET substrate, followed by coating a ZnO precursor as a protective layer to prepare the electrodes. The zinc oxide precursor comprises zinc acetate dissolved in ethanol and diluted lactic acid is subsequently added until the solution becomes transparent and colorless. The $Co(OH)_2$ nanosheets were electrochemically deposited on AgNWs using 0.01 M $Co(NO_3)_2 \cdot 6H_2O$ with a static potential of -1.0 V *versus* the standard calomel electrode (SCE). After being washed with DI water, the $Co(OH)_2$ nanosheets/AgNW hybrid electrodes were exposed to UV light (1 h) to enhance their stability. The transmittance of the hybrid electrode decreases with the increased deposition of $Co(OH)_2$. The high areal capacitance (5.18 mF cm^{-2}) was obtained at optimal loading of $Co(OH)_2$ (5 minutes) with ~75% transmittance (Fig. 8b). Also, this hybrid electrode retains 118% and 112% of initial areal capacitance after 10 000 and 20 000 charge–discharge cycles, respectively (Fig. 8c).[97] The synergetic effect of Ag and $Co(OH)_2$ nanosheets, the ZnO protecting layer, and UV irradiation treatments is the major reason for the outstanding cycling performance of the $Co(OH)_2$ nanosheets/AgNW based supercapacitor device.[97] Liu *et al.* have fabricated a transparent and

flexible all-solid-state supercapacitor using ultra-long (~75 μm) Ag nanowires which exhibit low sheet resistance (15.2 Ω sq^{-1}) with high transmittance (84%). The fabricated all-solid-state flexible supercapacitor ($PET/AgNWs/PEDOT:PSS/H_3PO_4/PVA/PEDOT:PSS/AgNWs/PET$) with a PEDOT:PSS protective layer has shown ~51% transmittance with a maximum areal capacitance of 0.9 mF cm^{-2} (device area ~ 1 cm^2) (see Fig. 8d and e).[98] On the other hand, AgNWs and $Ni/Co(OH)_2$ core–shell nanostructures fabricated by electrodeposition offer many advantages. It is interesting to note that a Ni–Co bimetal interface exists between AgNWs and $Ni/Co(OH)_2$. This interface (Ag NW@NiCo/NiCo(OH)$_2$) offers multiple advantages (Fig. 8f–h).[99] The Ni–Co layer improves the electron transport at the interfaces and acts as an interlayer to decrease the lattice mismatch. It further slows down the expansion of the hydroxide shell upon repeated charge–discharge cycles. In addition, upon exposure to an alkaline environment, the Ni–Co interface converts to $Ni/Co(OH)_2$, which helps increase the electrochemical performance. By properly tuning the ratio of Ni and Co, a high areal capacitance (22.2 mF cm^{-2}) was achieved.[99]

2.2.1.2. Carbon nanotubes (CNTs). Due to their excellent mechanical and electrical properties, besides natural abundance and low-cost, carbon nanotubes (CNTs) have been extensively used as alternative TCEs for many optoelectronic devices like touch screens,[100] loudspeakers,[101] and OLEDs.[102] Among various synthesis methods, solution-based deposition is preferred for SWCNT-based TCE fabrication due to its low-cost and scalable approach. However, the solution-based approach suffers from aggregation and high-contact resistance due to the different molecules attached to the SWCNT surface. In this context, Zhiqiang Niu *et al.* prepared SWCNT-based TCEs using the floating catalyst chemical vapor deposition (FCCVD) technique followed by a "repeated halving" approach. The major drawback of the simple FCCVD technique is the high minimum thickness of the prepared CNT film (>100 nm).[103] The repeated halving approach effectively reduces the thickness of the CNT film below 50 nm, improves the film's uniformity, and increases the utilization rate of SWCNTs. Transparent and symmetrical supercapacitors have been fabricated with such "repeated halving" CNTs on PET substrates (50 nm) which act both as an electrode and current collector, a transparent Nafion-117 membrane as a separator, and 1 M non-aqueous $LiClO_4$ as the electrolyte. The fabricated device exhibits a specific capacitance of 22.5 F g^{-1} with about 60% transmittance at 550 nm.[104] Similarly, CNTs prepared by the FCCVD technique were directly deposited onto both sides of the ionic liquid-based polymer electrolyte membrane, and the device showed high storage performance (Fig. 9a).[105] The excellent electrical conductivity of the prepared CNTs precludes using an external current collector. The device exhibits high power density (1370 kW kg^{-1}), high transmittance (70%) (Fig. 9b), and extraordinary electrochemical stability (94% capacitance retention over 20 000 cycles) (Fig. 9c).[105] In another example, SWCNT thin films were deposited onto a polymer PDMS substrate *via* vacuum filtration with a subsequent stamping process. The optical transmittance of the SWCNT electrode decreases from 82% to 56% with increasing mass loading of SWCNTs (0.02–0.08 mg). To
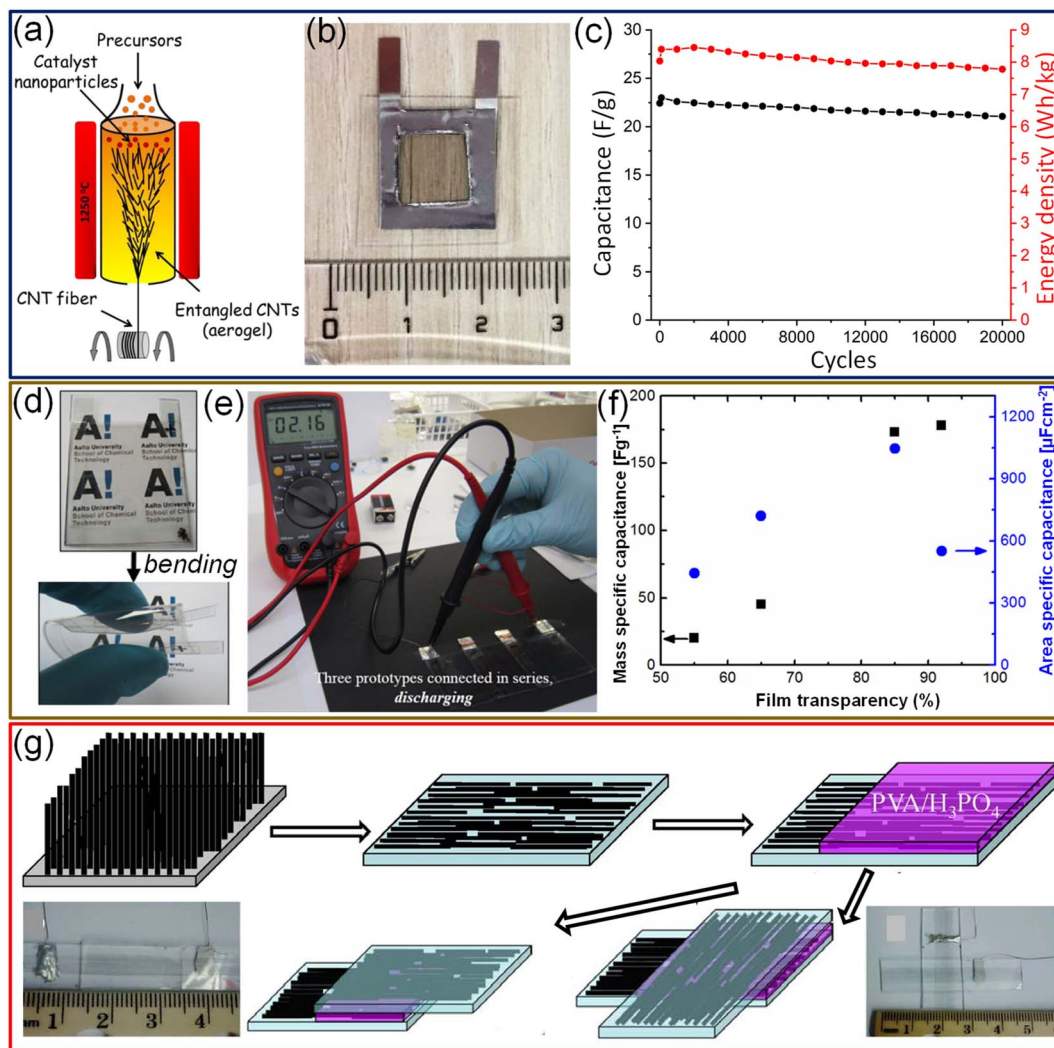
4920 | *J. Mater. Chem. A*, 2023, **11**, 4907–4936

This journal is © The Royal Society of Chemistry 2023

Fig. 9 Carbon nanotubes: (a) schematic representation of fabrication of CNT electrodes *via* the floating catalyst chemical vapor deposition technique. (b) Photograph of a free-standing transparent supercapacitor device. (c) The stability of the device tested for over 20 000 charge–discharge cycles. Reproduced from ref. 105 with permission from the Royal Society of Chemistry. (d) Photographs of a transparent flexible supercapacitor device fabricated with SWCNT thin films. (e) Photograph of three proto-type devices connected in series while discharging. (f) The dependence of areal and mass-specific capacitance on the SWCNT thickness. © IOP Publishing Ltd. Reproduced with permission. All rights reserved.[107] (g) Schematic diagram illustrating the fabrication process of a transparent and flexible supercapacitor using SWCNTs assembled in both parallel (bottom left) and cross (bottom right) configurations. Adapted with permission from ref. 108. Copyright 2014 by Springer Nature.

fabricate the supercapacitor, conducting carbon paste was used as an external current collector, SWCNTs as the electrode material, a Celgard-3401 as a separator, and TBAPF$_6$ (tetrabutylammoniumhexa-fluorophosphate) : PMMA (poly(methyl methacrylate)) : PC (propylene carbonate) : ACN (acetonitrile) in a ratio of 3 : 7 : 20 : 70 by weight as the electrolyte. The device fabricated with 0.02 mg SWCNT loading offers a specific capacitance of 22.2 F g^{-1} with about 82% transmittance.[106] Prototype flexible EDLCs with SWCNTs prepared by aerosol CVD exhibit extremely high specific capacitance (178 F g^{-1} or 552 μF cm^{-2}) with 90% transmittance and electrochemical stability for 10 000 cycles (Fig. 9d–f).[107] Chen *et al.* have demonstrated the fabrication of transparent ($\sim$75%) and flexible supercapacitors using highly aligned CNTs on a PDMS polymer substrate (Fig. 9g). The device can be biaxially stretched up to 30% strain without changing the electrochemical performance.[108]

Although SWCNTs are ideal for electrochemical double-layer capacitors (EDLCs) due to their high electrical conductance, chemical stability, and high surface area, the specific capacitance achievable with the EDLC mechanism is limited.[109] In this context, coating a conducting polymer or metal oxides as an overlayer improves the specific capacitance *via* a pseudo-capacitor or redox supercapacitor mechanism. While preparing transparent supercapacitors, it is necessary to keep the thickness of the materials lower to achieve higher transmittance. However, the sheet resistance of a 15 nm thin SWCNT film is relatively high (1500 Ω sq^{-1}). To fabricate SWCNT/PANI thin films on flexible substrates, SWCNT films were first transferred to a conducting FTO substrate, followed by
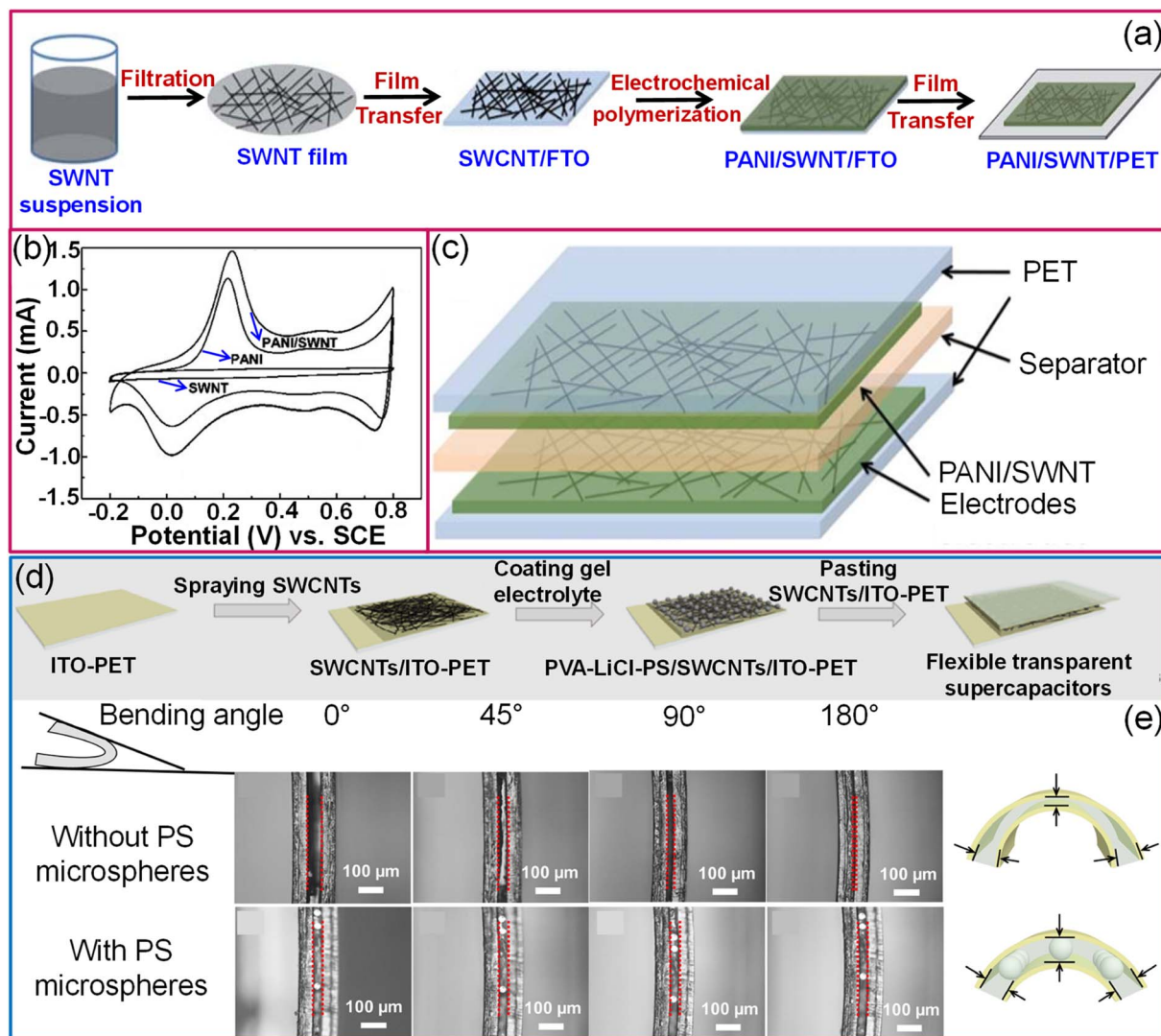
Fig. 10 Carbon nanotubes: schematic illustrations of fabrication of a transparent hybrid PANI/SWCNT electrode (a). (b) The contrast of cyclic voltammograms of pristine SWCNT, PANI and hybrid PANI/SWCNT electrodes and the supercapacitor device (c). Reproduced from ref. 109 with permission from the Royal Society of Chemistry. (d) Schematic representation of fabrication of a flexible transparent supercapacitor using a PVA–LiCl–PS electrolyte and SWCNT/ITO hybrid electrodes. (e) Schematic diagram and cross-sectional SEM images illustrating the stability of the device with PS microspheres in the electrolyte while bending. Reproduced with permission from ref. 110. Copyright 2020 American Chemical Society.

electrodeposition of polyaniline. Finally, SWCNT/PANI films were transferred to flexible and transparent PET substrates (Fig. 10a). Compared to pristine SWCNTs and PANI, SWCNT/PANI composite films evidently show better electrochemical performance (see Fig. 10b). A supercapacitor fabricated with SWCNT (10.0 mg cm^{-2})/PANI (59 wt%) electrodes offers a specific capacitance of 55 F g^{-1} (Fig. 10c).[109] Compared with the usage of only bare gel electrolytes between electrodes, the addition of monodispersed polystyrene microspheres helps control the spacing between electrolytes and protects the electrolyte from extrusion under deformation conditions (Fig. 10d and e).[110] Furthermore, MWCNTs/MnO$_2$ elevated the capacitance by at least an order of magnitude compared with SWCNTs.[110] The specific capacitance of the aligned MWCNT/PANI electrodes is 36 times that of bare MWCNT electrodes,

23 times that of pure PANI and three times that of randomly oriented MWCNT/PANI electrodes.[111]

2.2.1.3. Electrospun fibers. Non-conventional template-based methods have emerged for fabricating random mesh-like network electrodes. Towards this end, the free-standing, continuous nanofiber webs of polymers are produced by electrospinning and used as sacrificial templates for fabricating transparent electrodes. Metal is either physically evaporated or chemically deposited by electroplating on top of the fibers that are selectively dissolved, resulting in hollow nanotrough type fully interconnected nanostructures. The nanotrough geometry is shown to be advantageous since the electromagnetic cross-section is smaller, allowing extra visible light to pass through the electrode. The fiber width, length, and density could be controlled by tuning the electrospinning conditions.

4922 | *J. Mater. Chem. A*, 2023, **11**, 4907–4936

This journal is © The Royal Society of Chemistry 2023
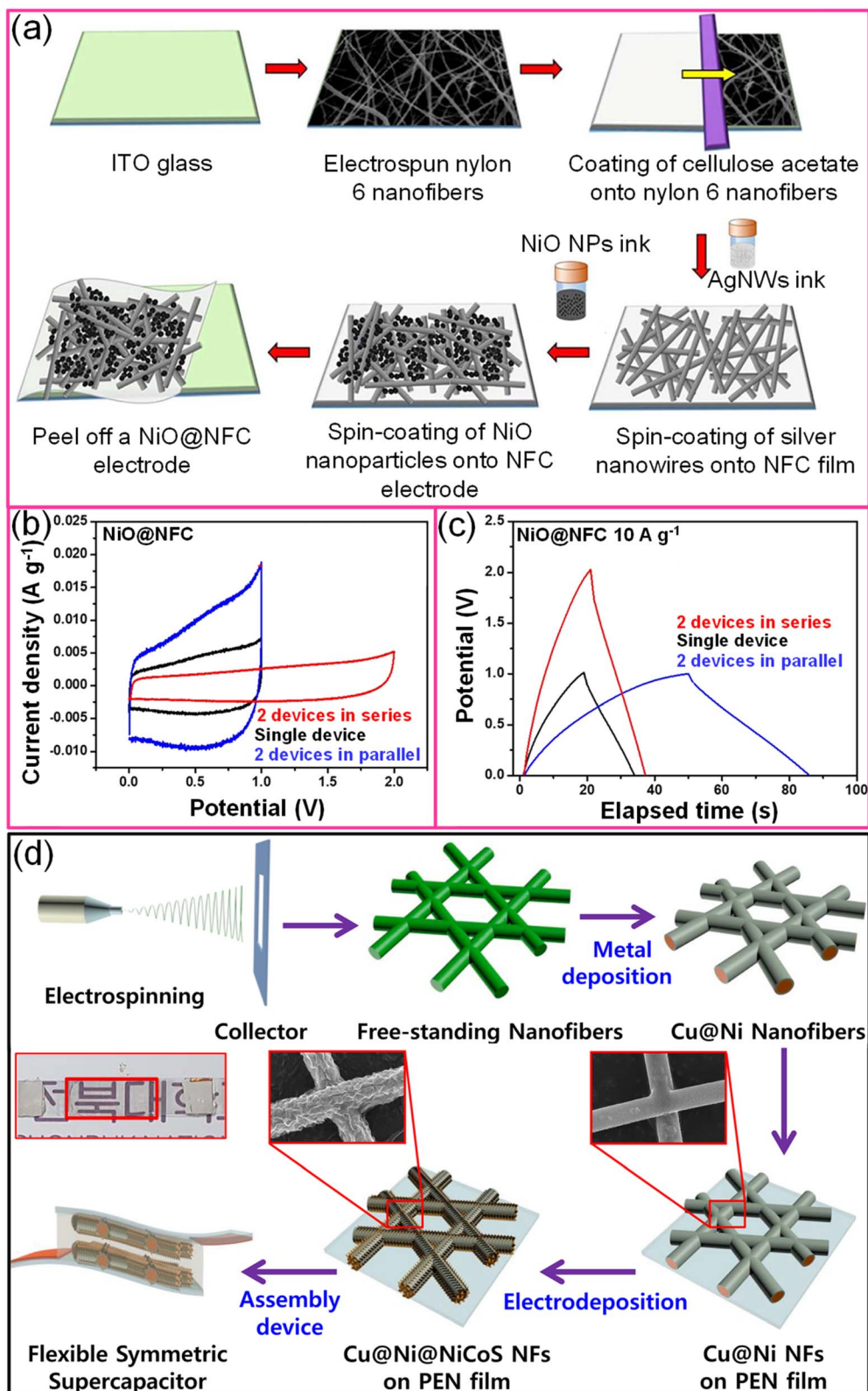
Fig. 11 Electrospun fibers: (a) schematic representation to fabricate the NiO@nanofiber composite (NFC) based flexible and transparent symmetric supercapacitor device. (b) Cyclic voltammogram and (c) galvanostatic charge–discharge curves of a single NiO@NFC device and two devices connected in both series and parallel. Reproduced with permission from ref. 113. Copyright 2020 American Chemical Society. (d) Schematic illustration for the preparation of a transparent supercapacitor device using Cu@Ni@NiCoS nanofibers using the electrospinning technique. Reprinted with permission from ref. 116. Copyright 2020 by Elsevier.

Undoubtedly, an extremely high transmittance of ~91% could be achieved at a very low R_S value of ~2 Ω sq^{-1}.

Electrospun nanofiber networks coated with metal result in a highly conducting and transparent metal network. For instance, An et al. realized a TCE of 90% transmittance with 0.36 Ω sq^{-1} sheet resistance by combining electrospun and electroplating techniques.[112] Besides offering excellent mechanical stability, the process is simple and eco-friendly.[113] Similarly, a flexible transparent supercapacitor fabricated using a nanofiber composite (NFC) electrode (NiO@NFC//NiO@NFC) exhibited excellent mechanical flexibility (10 000 bending cycles), high specific capacitance (160 F g^{-1}), optical transmittance (~75%) with maximum energy and power densities of 22 W h kg^{-1} and ~500 W kg^{-1}, respectively (Fig. 11a).[113] While connecting two supercapacitor devices in either series or parallel, the output potential and current, respectively, were improved compared to single devices (Fig. 11b and c). The MnO$_2$@Au NF network showed an areal capacitance of ~2 mF cm^{-2} with ~80% transmittance with a PVA/LiCl gel electrolyte.[114] A freestanding Au-coated PVA network was obtained by electrospinning PVA followed by Au metal deposition. The highly porous MnO$_2$ shell was electrodeposited under optimal conditions.[114] Similarly, extremely long MnO$_2$/Au stacked nanofiber networks on a PDMS substrate demonstrated a high areal capacitance (3.68 mF cm^{-2}) with nearly 60% transmittance and exhibited stability towards various deformations.[115] Besides simple oxides like MnO$_2$, battery-type ternary nickel-cobalt sulfide (NiCoS) can also be coated on the metal nanofiber network. For instance, the Cu@Ni@NiCoS nanofiber network acts both as the positive and negative electrodes and, while sandwiched with a PVA/KOH gel electrolyte, yielding high volumetric power (248 μW cm^{-3}) and energy densities (10.83 μW h cm^{-3}) with 65% transmittance (Fig. 11d).[116] In another example, an embedded PEDOT:PSS/AgNFs/NOA-63 hybrid transparent supercapacitor electrode was fabricated by a simple peel-off transfer technique that offered an areal capacitance of 0.91 mF cm^{-2} with ~78% transmittance.[70] The Ag deposited polymer nanofiber was initially transferred onto a PEDOT:PSS thin film and encapsulated with NOA-63. After UV curing, the PEDOT:PSS/AgNFs/NOA-63 film was carefully peeled off the Si substrate.[70]

2.2.2. Template-based networks. Parallelly, to overcome problems associated with networks, template-based lithography methods for the fabrication of meshes/grids have been adopted. The lithography-based methods are promising since they can produce patterns at desired locations with high reproducibility and accuracy. The feature sizes can be precisely controlled, and the choice of material can be tuned based on the requirement. Several lithography methods, such as photolithography and nanoimprint lithography, fabricate transparent conducting grids with periodic structures. The metallic networks fabricated via a template-based approach offer high conductivity, high stability, low fabrication cost, and large-area fabrication. In addition, the patterning technique is completely devoid of large junction resistance, the percolation threshold, and randomness.

2.2.2.1. Lithography techniques. Nanosphere lithography is a popular technique for fabricating patterned structures due to its simplicity, low cost, and large throughput. A transparent supercapacitor with an Au@MnO$_2$ core–shell structure was fabricated on a transparent flexible polymer substrate through nanosphere lithography and electrodeposition techniques. An Au mesh was developed on a PET substrate using a monolayer of hexagonally closely packed polystyrene spheres as a template, followed by reactive ion etching. Subsequently, the Au metal was deposited over the template, and polymer spheres were removed. The width of the Au mesh prepared on PET substrates entirely depends on the duration of ion etching. With increasing etching time, the resulting Au mesh width increases. Furthermore, electrodeposited MnO$_2$ is conformally coated over the electrodeposited Au nanomesh. The interconnected Au mesh acts as a transparent conducting electrode and holds the pseudocapacitive MnO$_2$ shell. The thickness of MnO$_2$ increases with the electrodeposition time. Finally, an Au@MnO$_2$ nanomesh-based transparent flexible supercapacitor was achieved by combining two such electrodes with a LiClO$_4$/PVA gel electrolyte. The device exhibited an areal capacitance of ~0.8 mF cm^{-2} with 40% transmittance (Fig. 12a–c).[117] An Au nanomesh was also obtained using the grain boundary lithography approach, which involves a bilayer lift-off metallization process.[118] The electrodeposited MnO$_2$ shell offers a high surface area and thus enhances the capacitance without significantly altering the transmittance (84.7%). The imperceptible supercapacitor exhibits high areal capacitance (0.53 mF cm^{-2}) with excellent stretchability and bending stability.[45] In an example, MnO$_2$ island-like arrays were fabricated by a breath-figure approach to fabricate a flexible transparent supercapacitor. Porous polystyrene-b-polyacrylic acid (PS-b-PAA) achieved by the breath-figure approach has been employed as a template for the MnO$_2$ growth over ITO/PET via electrochemical deposition followed by removal of the PS-b-PAA template to realize MnO$_2$ island arrays (Fig. 12d). The assembled MnO$_2$/ITO/PET supercapacitor device exhibited typical supercapacitor like CV characteristics (Fig. 12e) and offers ~5 mF cm^{-2} areal capacitance with an optical transmittance of 44% (Fig. 2f).[119]

In another approach, the patterned electrode grid, which occupies only a small fraction of the entire surface area, was developed using the soft lithography technique to offer high transparency to the supercapacitor device. While compared to other patterned electrodes, the transmittance of the full cell is significantly high due to the perfectly aligned electrodes. Highly transparent and flexible Ag/porous carbon or Ag/Ni$_x$Fe$_y$O$_z$@-RGO electrodes featuring a hexagonal grid-like morphology were fabricated using a PDMS stamp prepared via photolithography. Initially, PDMS stamps and PET substrates were cleaned with O$_2$ plasma to enhance the wettability of precursor inks. After pressing the stamps against PET substrates, precursor Ag ink was injected around the stamp's edges, and it flowed inside the mold by capillary force. The temperature was slowly increased to 130 °C to dry the precursor and to improve the conductivity of the Ag mesh. At this stage, the stamp is not

4924 | J. Mater. Chem. A, 2023, **11**, 4907–4936

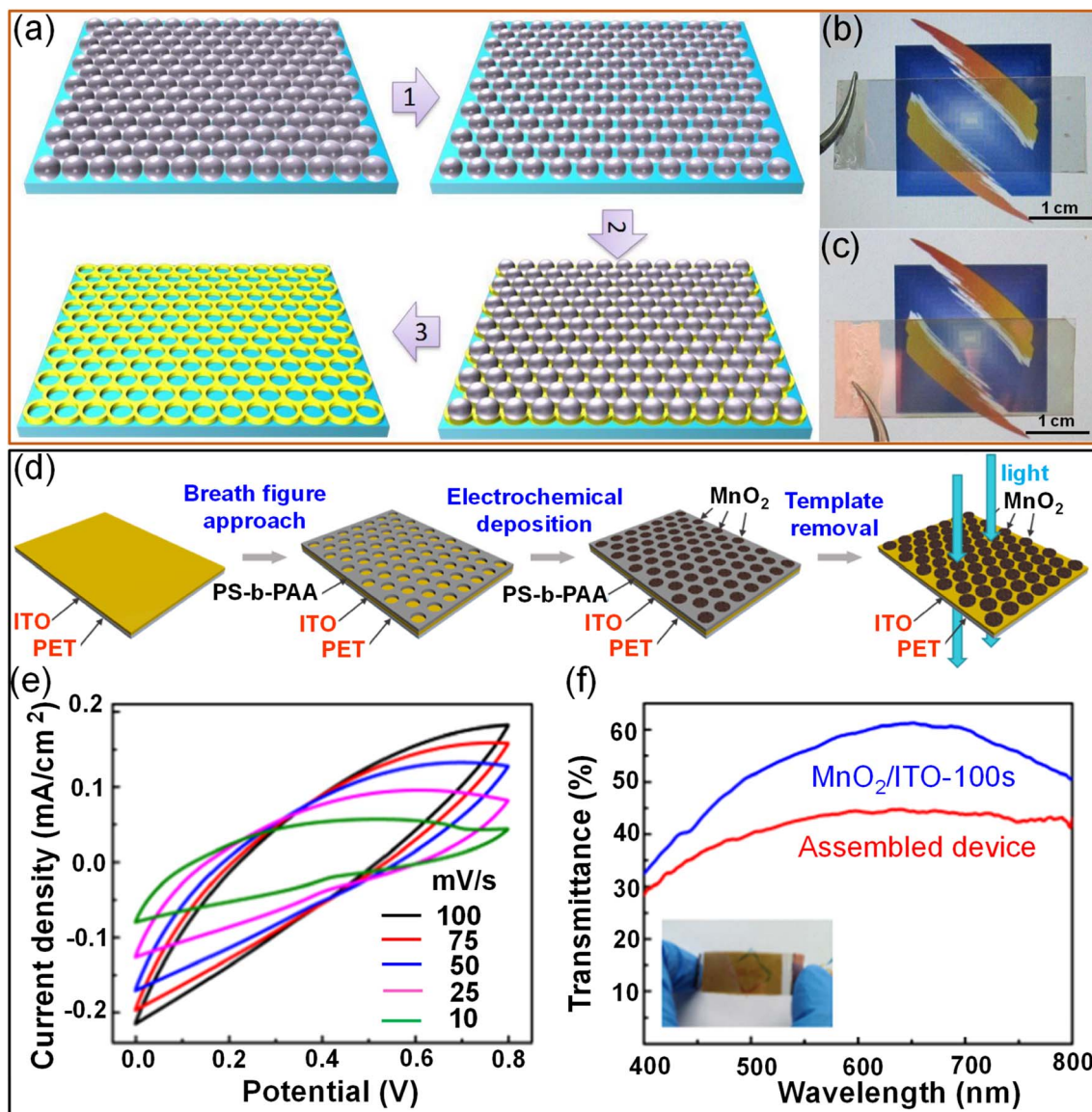This journal is © The Royal Society of Chemistry 2023

Fig. 12 Lithography: (a) the synthetic procedure for preparing the Au nanomesh film through nanosphere lithography followed by reactive ion etching. Photographs of (b) the Au/PET film and (c) the Au@MnO$_2$/PET film. Reproduced with permission from ref. 117. Copyright 2014 by John Wiley and Sons. (d) Schematic illustration of the fabrication of MnO$_2$ island array electrodes using a breath-figure polymer pattern as a template for oxide growth. (e) CV curves of the fabricated supercapacitor device at various scan rates ranging from 10 to 100 mV s^{-1}. (f) Transmittance spectra of the MnO$_2$/ITO-100 s electrode and the assembled supercapacitor device (inset image). Reproduced with permission from ref. 119. Copyright 2018 American Chemical Society.

filled with the Ag ink; thus, the active electrode precursor ink was injected around the stamp's edges. Finally, the PDMS stamp was carefully removed to realize Ag/porous carbon or Ag/Ni$_x$Fe$_y$O$_z$@RGO electrodes on transparent and flexible substrates. The Ag film exhibits ~88% transmittance (7.6 Ω sq^{-1}), which is further reduced to 85–86% due to the coating of carbon electrode materials. The areal capacitance and transmittance of the fully assembled supercapacitor device are 226.8 μF cm^{-2} and 70.6%, respectively.[120]

A freestanding, highly transparent (>84%), and conductive (3 × 10^4 S cm^{-1}) Ni network was obtained *via* a direct-write laser micro-patterning technique followed by selective electrodeposition. The thickness of the freestanding mesh can be tailored

in the range of 1.5–5 μm by varying the electrodeposition duration. The MnO$_2$ pseudocapacitive material was electrodeposited to increase the surface area of the electrode, which in turn increases the device's capacitance. The transparent Ni network can be attached to arbitrary objects such as pencils, leaves, and Rubik cubes. The electrochemical energy storage performance of the MnO$_2$@Ni network electrode was examined using a PVA/LiCl gel electrolyte. The device achieved high transmittance (~80%) and capacitance values (10.6 mF cm^{-2}) due to MnO$_2$ coating, besides offering superior flexibility.[121] In another example, a Ni mesh/PEDOT:PSS hybrid was employed as the active electrode material for all-solid-state, flexible supercapacitors. The typical width and thickness of the metallic

This journal is © The Royal Society of Chemistry 2023

J. Mater. Chem. A, 2023, **11**, 4907–4936 | **4925**

Ni ribbon are 3–5 μm and 0.8–3.5 μm, respectively. At the same time, the thickness can be precisely controlled by varying the deposition duration. The supercapacitor device showed ∼83% transmittance and high areal capacitance (0.52 mF cm^{-2}) with excellent stability towards deformation.[122] Xu *et al.* have fabricated an embedded Ag grid/PEDOT:PSS hybrid electrode by a facile soft UV imprinting lithography technique coupled with a scrap technique. Firstly, the direct laser writing technique patterned the photoresist layer into brick-wall grooves. Secondly, the patterned structure is transferred to a soft polyurethane acrylate mold and later to UV-curable resin *via* ultraviolet-nano-imprint lithography (UV-NIL). The UV-curable resin (D10, PhiChem) was cured by exposing it to UV light for just 2 s (1000 mW cm^{-2}). Subsequently, Ag nanoparticle ink was drop cast on the UV resin layer, and nanoparticles were filled into grooves using the scrap technique, followed by annealing at
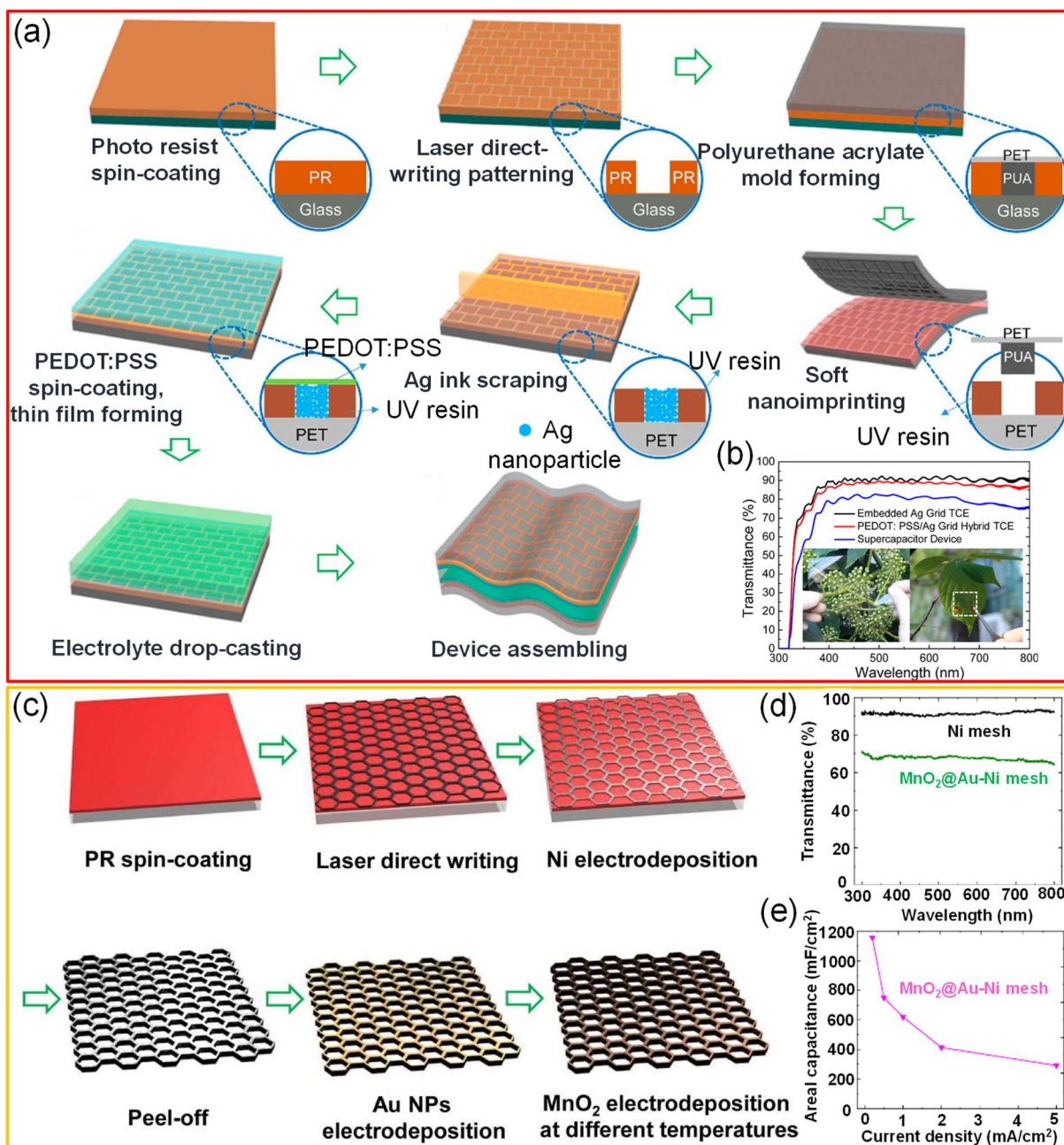
Fig. 13 Lithography: (a) schematic representation of the fabrication of a flexible transparent solid-state supercapacitor using an embedded Ag grid TCE. (b) Transmittance spectra of the Ag grid TCE, the PEDOT:PSS/Ag grid hybrid TCE, and the supercapacitor device. Insets show the digital photographs of transparent supercapacitor devices prepared using the Ag grid TCE. Reproduced with permission from ref. 41. Copyright 2017 American Chemical Society. (c) Schematic illustration of fabricating a self-standing core−shell MnO$_2$@Au−Ni mesh electrode. (d) Transmittance spectra of Ni mesh and MnO$_2$@Au−Ni mesh electrodes. (e) The graph representing the relationship of areal capacitance with current density for the MnO$_2$@Au−Ni mesh electrode. Reproduced with permission from ref. 123. Copyright 2019 American Chemical Society.

4926 | *J. Mater. Chem. A*, 2023, **11**, 4907–4936

This journal is © The Royal Society of Chemistry 2023

80 °C. Finally, the embedded Ag/PEDOT:PSS electrode was realized by spin-coating PEDOT:PSS solution onto Ag grid electrodes. A flexible transparent all-solid-state supercapacitor was obtained by pressing two Ag/PEDOT:PSS electrodes with a PVA/H$_3$PO$_4$ gel electrolyte. The fabricated supercapacitor offers high transmittance ($\sim$80%) with high areal capacitance (2.79 mF cm^{-2}) and retains around 92% of initial capacitance even after 10 000 cycles of charging and discharging (Fig. 13a and b).[41] Liu *et al.* fabricated a high-performance solid-state symmetric supercapacitor device (MnO$_2$@Au–Ni mesh) with an areal capacitance of 78.5 mF cm^{-2} and an optical transmittance of 61%. In this process, self-standing hexagonal patterns of Ni were created by laser direct writing followed by selective electrodeposition of Ni. Further Au nanoparticles (nano-glue between Ni and MnO$_2$) were electrodeposited, followed by MnO$_2$ to realize transparent core–shell microstructures (see Fig. 13c–e). The electrode has shown an excellent areal capacitance of 1.15 F cm^{-2} (transmittance $\sim$ 70%).[123]

Amidst multiple advantages, the biggest drawback associated with lithography-based techniques is the cost of the master, resist, and developer, along with the laborious processing steps. The nanoimprinting process requires a hard master, and a resist that is hard baked, followed by metal deposition. This has limited the use of lithography techniques in TCE fabrication. Another challenge is scalability since large contact areas between the mold and the imprinted nanostructures can result in sticking issues. Moreover, the pattern fidelity is compromised over large areas as the polymer chains in the active material tend to relax elastically. Most conventional lithography techniques are also unsuitable for directly fabricating nanostructures on flexible, curved, and rough surfaces.

2.2.2.2. Self-forming process. The choice of the templating method is crucial in determining the properties of the resulting transparent conducting electrode. A versatile approach based on a crack template was developed to fabricate a fully interconnected network. Interestingly, the method is termed a self-forming or spontaneously crackled template in parallel efforts from Han *et al.*[124] and Kulkarni and coworkers,[125–130] respectively. Both groups have demonstrated the fabrication of high-performance transparent electrodes by fine-tuning the control over the cracking process such that the metal network obtained after removing the sacrificial template is a fully interconnected network with a high transmittance of $\sim$85% and sheet resistance of $\sim$10 Ω sq^{-1}. Meanwhile work carried out by Han *et al.* involved spin coating, which is restricted to the limited size of the substrate.[124] Nevertheless, Kulkarni and co-workers demonstrated the formation of a crack template over a much wider length scale that can be fabricated on flat, flexible as well
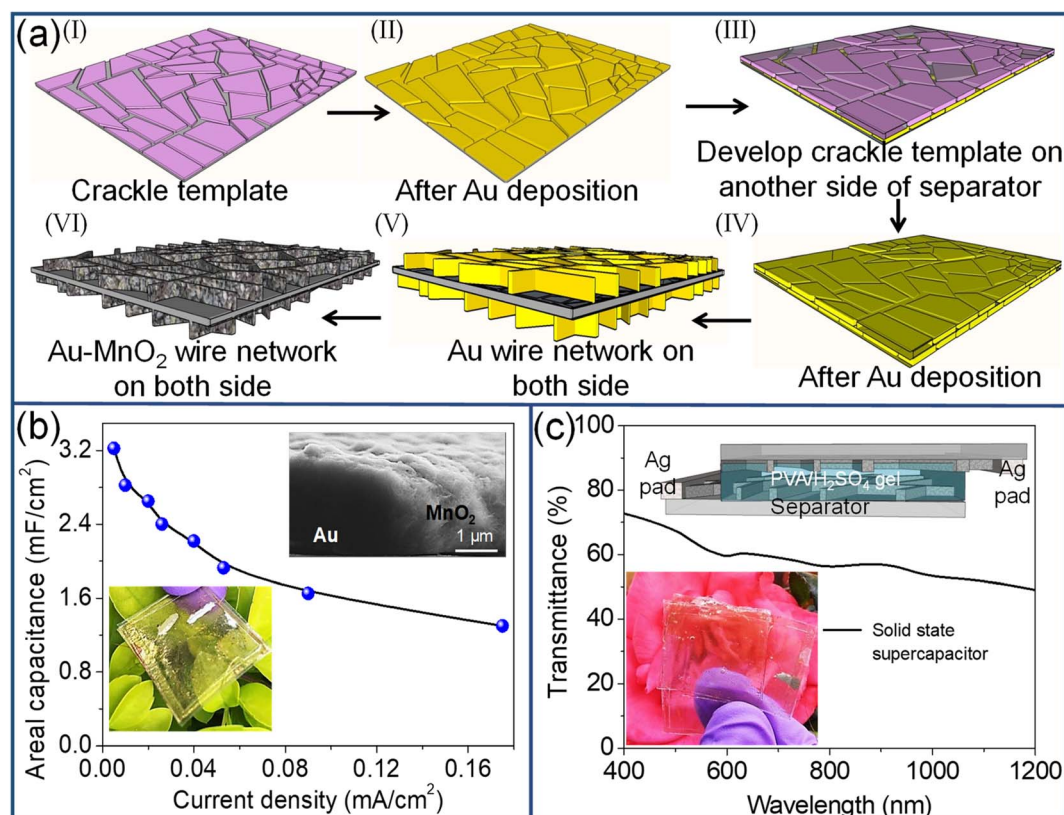
Fig. 14 Self-forming process: (a) schematic representation to fabricate a core−shell Au/MnO$_2$ network using a crackle template. (b) A graph showing the areal capacitance of the Au/MnO$_2$ supercapacitor electrode *versus* its discharging current densities. The insets in (b) show the SEM images of the fabricated Au/MnO$_2$ nanowire mesh and the device's photograph. (c) The solid-state supercapacitor of the Au/MnO$_2$ electrode device (bottom) shows a transmittance of 78%, and the inset shows a schematic of a solid-state supercapacitor device. Reproduced with permission from ref. 125. Copyright 2017 by John Wiley and Sons.

This journal is © The Royal Society of Chemistry 2023

J. Mater. Chem. A, 2023, **11**, 4907–4936 | **4927**

Table 1 Summary of optical and electrochemical performances of transparent supercapacitors fabricated with different transparent electrodes[a]

Electrode material for transparent supercapacitors	Active materials	Electrolyte	Transmittance	Capacitance	Energy density	Power density	Ref.
Ultra-thin conducting networks							
Graphene	Ultrathin graphene films	2 M KCl	70% (550 nm)	135 F g^{-1}	15.4 W h kg^{-1}	554 W kg^{-1}	55
	CVD-grown graphene bilayers and redox-active interlayer	PVA/H$_2$SO$_4$	75% (550 nm)	101 μF cm^{-2}	~0.02 W h cm^{-3}	90 W cm^{-3}	57
	Graphene sheets *via* rapid thermal annealing (RTA)	PVA/H$_3$PO$_4$	~67% (500–800 nm)	12.4 μF cm^{-2}	2.94 W h kg^{-1}	438.6 kW kg^{-1}	63
	Free-standing flexible graphene paper grown using NaCl as a template	PVA/H$_2$SO$_4$	59% (800 nm)	3.3 mF cm^{-2}	430 μW h cm^{-3}	190 mW cm^{-3}	42
	Single layer graphene *via* thermal CVD	Polyacrylonitrile electrospun mat soaked in PVA–LiCl	~59% (550 nm)	3.83 μF cm^{-2}	—	—	141
Organic thin films	Free-standing PEDOT:PSS *via* facile multilayer spin-coating	PVA/H$_3$PO$_4$	~60% (550 nm)	~4.72 mF cm^{-2}	0.38 mW h cm^{-2}	0.036 W cm^{-2}	68
	PEDOT: PSS in formic acid	0.5 M K$_2$SO$_4$ (aq.)	70% (550 nm)	1.9 mF cm^{-2}	—	—	25
Metal oxides	Polypyrrole	H$_3$PO$_4$/PVA	71% (550 nm)	1.64 mF cm^{-2}	5 mW cm^{-3}	67.3 mW h cm^{-3}	40
	ITO	1-Butyl-3-methylimidazolium chloride and cellulose	92% (450–800 nm)	~18 F g^{-1}	—	—	77
	ITO/Co$_3$O$_4$	PVA/H$_3$PO$_4$	51% (550 nm)	6.03 mF cm^{-2}	3.01 W h kg^{-1}	1.152 kW kg^{-1}	78
	ITO/MnO$_2$	1 M Na$_2$SO$_4$	77.4% (550 nm)	9.2 mF cm^{-2}	—	10.1 kW kg^{-1}	80
	MnO NP/TC/ITO NP/TC	0.5 M Na$_2$SO$_4$	60.8% (550 nm)	40.5 mF cm^{-2}	0.82 μW h cm^{-2}	113 μW cm^{-2}	81
	Coaxial RuO$_2$-ITO nanopillars	0.5 M H$_2$SO$_4$	~60% (550 nm)	1235 F g^{-1}	—	—	82
	AZO/NiO	PVA/KOH	83% (550 nm)	3.4 mF cm^{-2}	45.38 nW h cm^{-2}	4.97 μW cm^{-2}	85
	MoO$_3$ nano-paper	PVA/LiCl	~90% (400–800 nm)	~258 F g^{-1}	22.89 W h kg^{-1}	10.1 kW kg^{-1}	86
MXenes	Ti$_3$C$_2$T$_x$	PVA/H$_2$SO$_4$	~80% (550 nm)	0.86 mF cm^{-2}	0.011 μW h cm^{-2}	0.62 μW cm^{-2}	39
MOFs	Ni$_3$(HITP)$_2$	PVA/KCl	55.8% (550 nm)	1.35 mF cm^{-2}	0.05 μW h cm^{-2}	1.25 μW cm^{-2}	95
Metal nanowires	AuNWs	PVA/KNO$_3$ and PVA/ H$_3$PO$_4$	79% (550 nm)	226.8 μF cm^{-2}	—	—	96
Non-template based							
Carbon nano-tubes	SWCNT	1 M LiClO$_4$	60% (550 nm)	22.5 F g^{-1}	12.5 W h kg^{-1}	13.9 kW kg^{-1}	104
	CNT fibre aerogels	(Pyr$_{14}$TFSI):(PVDF-*co*-HFP)	70% (550 nm)	29 F g^{-1}	10 W h kg^{-1}	1370 kW kg^{-1}	105
	SWCNT	TBAPF$_6$:PMMA:PC:ACN	82% (550 nm)	34.2 F g^{-1}	18 kW h kg^{-1}	21.1 kW kg^{-1}	106
	SWCNT	PVA/H$_3$PO$_4$	92% (550 nm)	552 μF cm^{-2}	—	—	107
	CNT/PDMS	PVA/H$_3$PO$_4$	~75% (550 nm)	7.3 F g^{-1}	1 W h kg^{-1}	1.1 kW kg^{-1}	108
	SWCNT/PANI	1 M H$_2$SO$_4$	70% (550 nm)	55 F g^{-1}	—	—	109
	MWCNTs/MnO$_2$	PVA/LiCl	52.3% (550 nm)	1.7 mF cm^{-2}	—	—	110
	MWCNT/PANI	H$_3$PO$_4$/PVA	70% (300–900 nm)	233 F g^{-1}	—	—	111
Electrospun fibers	MnO$_2$@Au nanofibers	PVA/LiCl	~80% (400–800 nm)	~2 mF cm^{-2}	0.14 μW h cm^{-2}	4 μW cm^{-2}	114
	MnO$_2$/Au nanofiber networks	LiClO$_4$/PVA	60% (550 nm)	3.68 mF cm^{-2}	56 μW h cm^{-2}	0.32 μW cm^{-2}	115
	Cu@Ni@NiCoS	PVA/KOH	65% (550 nm)	1.21 μA h cm^{-2}	10.83 μW h cm^{-3}	248 μW cm^{-3}	116
Template based							
Lithography	Au@MnO$_2$ core-shell	LiClO$_4$/PVA	40% (550 nm)	~0.8 mF cm^{-2}	—	—	117
	Au@MnO$_2$ nanomesh electrodes	PVA/Na$_2$SO$_4$	82% (550 nm)	0.53 mF cm^{-2}	0.047 μW h cm^{-2}	2.16 μW cm^{-2}	45
	MnO$_2$@Ni network	PVA/LiCl	~80% (550 nm)	10.6 mF cm^{-2}	—	—	121
	MnO$_2$/ITO/PET	PVA/LiCl	44% (550 nm)	4.73 mF cm^{-2}	—	—	119

Review

Table 1 (Contd.)

Electrode material for transparent supercapacitors	Active materials	Electrolyte	Transmittance	Capacitance	Energy density	Power density	Ref.
Self-forming	MnO₂@Au–Ni mesh	PVA/LiCl	61.1% (550 nm)	78.46 mF cm⁻²	—	—	123
	MnO₂@Au	1 M Na₂SO₄	~75% (550 nm)	3.2 mF cm⁻²	~2 mW h cm⁻³	~2 W cm⁻³	125
	MoS₂@Ni and MnO₂@Ni	LiCl/PVA	~50% (550 nm)	2.42 mF cm⁻²	~0.86 µW h cm⁻²	16 µW cm⁻²	131
Hybrid	Tungsten oxide nanoflakes/nitrogen doped graphene quantum dots	PVA/H₃PO₄	70% (400–800 nm)	178.82 F g⁻¹	15.8 W h kg⁻¹	360.1 W kg⁻¹	62
	Graphene/CNTs/AgNW	PVA/H₃PO₄	64% (550 nm)	~0.31 mF cm⁻²	25.5 nW h cm⁻²	1.25 µW cm⁻²	56
	AgNWs/Ni(OH)₂–PEIE/PEDOT:PSS	PVA/LiCl	80% (550 nm)	3.3 mF cm⁻²	0.074 µW h cm⁻²	3.2 µW cm⁻²	69
	PEDOT:PSS/AgNFs/NOA 63	H₂SO₄/PVA	77.4% (550 nm)	0.91 mF cm⁻²	2.31 mW h cm⁻³	0.13 W cm⁻³	70
	Ag/Au/polypyrrole	PVA/H₃PO₄	73% (550 nm)	580 µF cm⁻²	~10 W h kg⁻¹	~1000 W kg⁻¹	76
	Au/graphene composites	PVA/H₃PO₄	~75% (520 nm)	~82 µF cm⁻²	—	—	61
	ITO/PEDOT	PVP/LiClO₄	~50% (370–770 nm)	15 F g⁻¹	—	—	83
	In₂O₃ nanowires and CNT composites	1 M LiClO₄	~65% (550 nm)	64 F g⁻¹	1.29 W h kg⁻¹	7.48 kW kg⁻¹	84
	SWCNT and Ti₃C₂Tₓ TCEs	PVA/H₂SO₄	72% (550 nm)	1.6 mF cm⁻²	0.05 µW h cm⁻²	2.4 µW cm⁻²	39
	Ni₃(HITP)₂//PEDOT:PSS	PVA/KCl	61% (550 nm)	1.06 mF cm⁻²	0.12 µW h cm⁻²	1.35 µW cm⁻²	95
	Co(OH)₂ nano-sheets/Ag nanowires	PVA/PAAS/KCl	54% (550 nm)	5.18 mF cm⁻²	0.04 µW h cm⁻²	28.8 µW cm⁻²	97
	PET/AgNWs/PEDOT:PSS/H₃PO₄/PVA/PEDOT:PSS/AgNWs/PET	H₃PO₄/PVA	~51% (550 nm)	0.273 mF cm⁻²	~1.5 W h kg⁻¹	~300 W kg⁻¹	98
	Ag NW@NiCo/NiCo(OH)₂	PVA/LiClO₄/KOH	54.3% (550 nm)	22.2 mF cm⁻²	3.0 W h kg⁻¹	3.5 W kg⁻¹	99
	Ni mesh/PEDOT:PSS	PVA/H₃PO₄	~83% (550 nm)	0.52 mF cm⁻²	—	—	122
	Ag grid/PEDOT:PSS	PVA/H₃PO₄	~80% (550 nm)	2.79 mF cm⁻²	—	—	41
	Ag/porous carbon and Ag/NiₓFeᵧO₂@reduced graphene oxide	PVDF–HFP/LiTFSI	70.6% (550 nm)	226.4 µF cm⁻²	2.7 mW h L⁻¹	1002.5 mW h L⁻¹	120
Flexible TMSC	MnO₂/CNT	[BMIM][TFSI]/PMMA	~80% (550 nm)	12.6 mF cm⁻²	0.04 µW h cm⁻²	7.94 µW cm⁻²	143
	PANI@ITO and PANI/CNT	PVA/H₂SO₄	—	140 F g⁻¹	—	—	147
	AgNW/PEDOT:PSS/PU	PVA/H₃PO₄	~75% (550 nm)	190 µF cm⁻²	—	—	142
	Graphene via inkjet printing technology	PVA/H₃PO₄	87% (550 nm)	12.6 µF cm⁻²	—	—	135
	Ag nanowires and MoS₂ nanosheets	PVA/H₂SO₄	~77.5% (550 nm)	27.6 mF cm⁻²	2.453 µW h cm⁻²	1.472 mW cm⁻²	136
	Carbon NPs/Ni-based micro-supercapacitor	1 M Et₄NBF₄/propylene carbonate	45% (400–1100 nm)	2.89 F g⁻¹	—	—	137

^{a} Transparent micro-supercapacitor (TMSC), nanoparticle (NP), tricarballylicacid (TC), nanowires (NW), and nanofibers (NF).
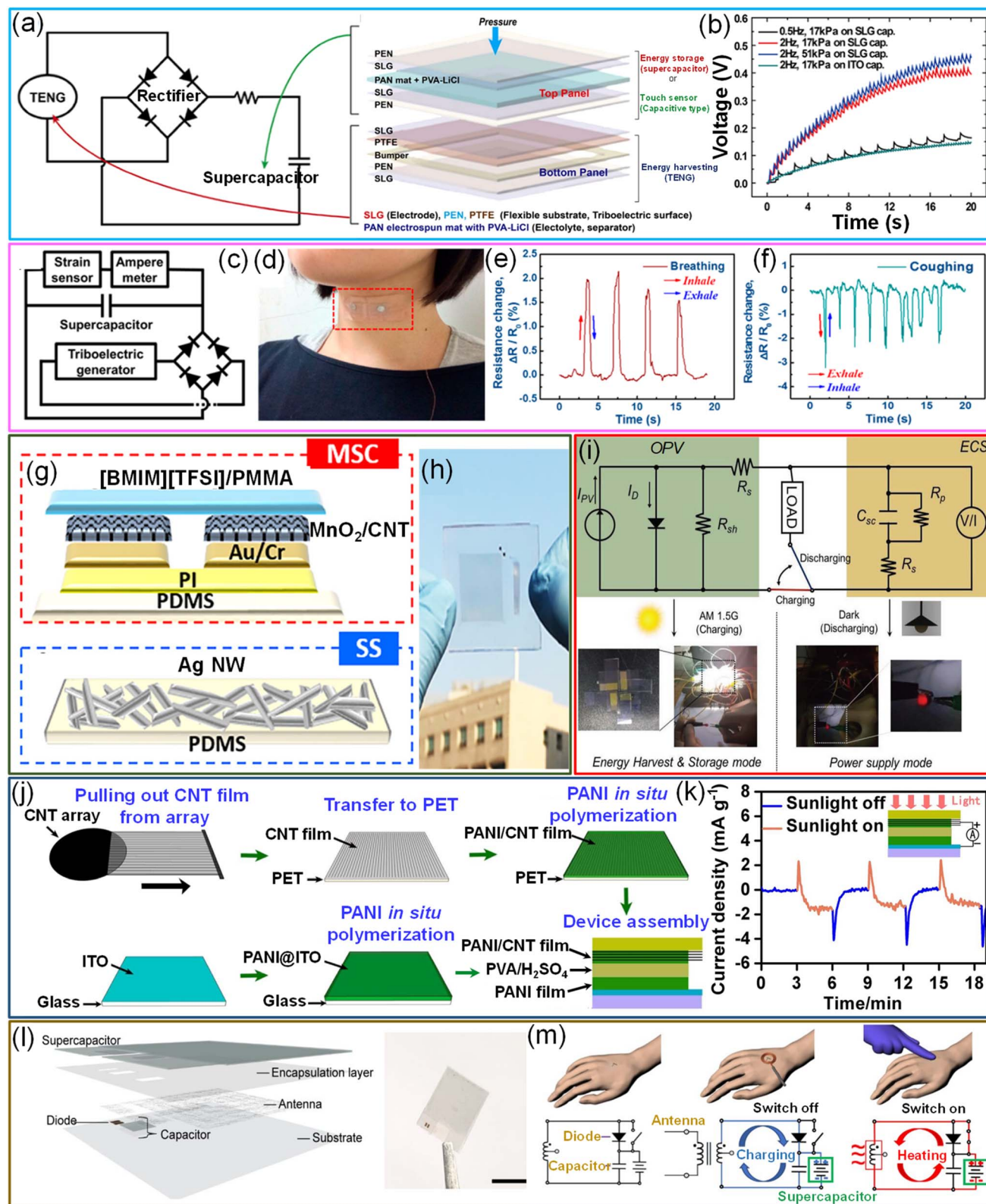
Fig. 15 Applications of transparent supercapacitors. (a) A rectifying-bridge circuit diagram integrating an energy harvesting triboelectric nanogenerator (TENG) with an energy-saving supercapacitor fabricated using single-layer graphene (SLG) electrodes. (b) The charging voltage *vs.* time curve for various applied frequencies (0.5 and 2 Hz) and forces (17 and 51 kPa) towards the TENG device to charge the supercapacitor. The ITO-based capacitor was used as the reference. Reproduced with permission from ref. 141. Copyright 2019 American Chemical Society. (c) The electrical circuit diagram shows the integration of the strain sensor with the supercapacitor and TENG devices using a rectifier. The AgNW/PEDOT:PSS/PU nanocomposite was employed as an active material for the fabrication of all three devices. (d) Photograph illustrating the transparency of the fabricated strain sensor attached to the neck. (e) and (f) Resistance variation for the strain sensor upon breathing and

4930 | *J. Mater. Chem. A*, 2023, **11**, 4907–4936

This journal is © The Royal Society of Chemistry 2023

as curved surfaces and named it Crackle Lithography (CL).[125–130] The scalability and uniformity of crackle templates over A4 size areas and even bigger are achieved by adopting several different coating processes, such as spray coating, roll coating, rod coating, drop coating *etc.* and are well established in the literature. Kiruthika *et al.* fabricated a transparent supercapacitor using the CL method in which highly interconnected spontaneously formed crackles were used as a template for electrode fabrication. Besides high interconnectivity among the crackles over a large area, crackles are down to the substrate and devoid of residual crackle precursors (acrylic resin).[125] While depositing Au metal, the deposition occurs over the crackle template and inside cracks (*i.e.*, substrate). After removing the template, an interconnected Au network with seamless junctions was achieved on the desired separator substrate. The transmittance and sheet resistance of the electrode could be fine-tuned by varying the width and density of the crackles and by the thickness of the metal, respectively. The electrochemically deposited MnO_2@Au enhances the surface area and electrochemical capacitance. In place of sandwiching electrodes with a separator, the electrodes were developed on both sides of the separator substrate, resulting in a lightweight supercapacitor. The device exhibited high areal capacitance (3.2 mF cm^{-2}) and transmittance (78%) with excellent cycling stability, as shown in Fig. 14.[125] In another study, transparent MoS_2@Ni and MnO_2@Ni mesh-based transparent asymmetric supercapacitors were fabricated on a plastic substrate *via* the crackle template approach (silica template). A maximum areal capacitance of 2.42 mF cm^{-2} with ~50% transmittance with excellent mechanical stability was achieved.[131] Metal-based hybrid TCEs have shown superior performance and attracted worldwide attention.[132,133] Commonly used metals Ag, Au and Cu have mainly been utilized to fabricate transparent electrodes due to their high electrical conductivity, availability, and ease of processing.

3. Flexible transparent micro-supercapacitors

From basic research and practical applications, lightweight and flexible micro-energy storage devices that can be integrated into circuits have become more crucial to meet the requirements of flexible, multifunctional, and wearable electronics.[134] The micro-supercapacitor (MSC) device aims to avoid heavy packaging, improve transparency and facilitate integration in portable electronics. Sollami Delekta *et al.* developed graphene-based interdigitated electrodes for flexible transparent MSCs *via* inkjet printing. 7-layer graphene interdigital electrodes with a 600 μm width, 2.5 mm length, and 200 μm spacings were coated with a PVA/H_3PO_4 gel electrolyte for flexible transparent supercapacitors. The device offers high transmittance (87%) with excellent bending stability (91.3%) with a maximum areal capacitance of 12.6 μF cm^{-2}.[135] To fabricate MSCs with more inherent mechanical flexibility, high-rate capacity, and cycling stability, Li *et al.* employed AgNWs–MoS_2 based hybrid interdigitated electrodes with a width and interspacing of 1000 and 25 μm, respectively, using a direct laser writing approach. The fabricated in-plane micro-supercapacitors demonstrated ~77.5% transmittance with high specific areal capacitance (27.6 mF cm^{-2}) and retained 96.4% capacitance even after 10 000 charge–discharge cycles.[136] Yu and coworkers created carbon nanoparticles/Ni-based micro-supercapacitors by depositing carbon nanoparticles on a finger-type Ni current collector. Finally, the devices were assembled using gel electrolytes, yielding a capacitance of 2.89 F g^{-1} with nearly 45% transmittance. Because of their outstanding performance, the fabricated device can be used in flexible electronics.[4,137] Direct write methods, including inkjet printing and laser ablation of conducting films, have been developed as alternative high throughput, low-cost methods.[138] Some of them are even adaptable to large-area processing. In any case, a micro-supercapacitor has the option to attain higher capacitance by stacking up along the third dimension laterally while maintaining a desired value of transmittance. Still, the printed features are much wider, of the order of tens and hundreds of microns, which obstructs the visibility and deteriorates the current collection efficiency of electrodes. These are usually integrated with ultrathin films of metal, ITO, graphene, or PEDOT:PSS as hybrid electrodes for improved charge storage properties.[138] However, if a continuous thin film is grown thick laterally, the charge storage sites beneath the top layers may become inaccessible by the ions, thus increasing the resistance and limiting the capacitance.[25] Nevertheless, a junction-free, fully interconnected network in the form of an aperiodic mesh is highly advantageous. Table 1 summarizes the optical and electrochemical performances of various transparent supercapacitors discussed so far.

coughing, respectively, measured using a supercapacitor charged by a TENG. Reproduced with permission from ref. 142. Copyright 2015 American Chemical Society. (g) The cross-sectional view of a transparent and stretchable energy storage micro-supercapacitor (MSC) device for driving an integrated strain sensor (SS) and (h) its photograph. Reprinted with permission from ref. 143. Copyright 2020 by Elsevier. (i) The electrical circuit diagram of semitransparent energy storing functional photovoltaics (energy harvesting) connected with an electrochromic supercapacitor (energy storing) (top). The pictures shown in the bottom correspond to glowing red LED light using the energy stored by the supercapacitor through photovoltaics upon illumination. Reproduced with permission from ref. 139. Copyright 2020 by John Wiley and Sons. (j) Schematic representation of the fabrication of a polymer supercapacitor capable of self-charging under sunlight. (k) The variation in current density with time while illuminating the device with AM 1.5 solar illumination (power density ~ 1000 W m^{-2}) (red line) and under no illumination (blue line) without any external voltage bias. Reproduced with permission from ref. 147. Copyright 2015 American Chemical Society. (l) Schematic illustrating the integration of a supercapacitor with rectifiers and antennas. The photograph on the right is a transparent flexible, and wirelessly rechargeable heat patch. The scale bar corresponds to 1 cm. (m) Schematic representation denoting the change in the circuit diagram of the heat patch while under wirelessly charging and discharging cycles. Reproduced with permission from ref. 148. Copyright 2020 American Chemical Society.

This journal is © The Royal Society of Chemistry 2023

J. Mater. Chem. A, 2023, **11**, 4907–4936 | **4931**

4. Applications of transparent supercapacitors

Transparent supercapacitors find enormous applications combined with solar cells and other functional devices.[92,139,140] For instance, Chun et al. fabricated self-charging power and touch-sensing systems using single-layer graphene-based electrodes (Fig. 15a).[141] The schematic on the right shows that the top panel performs a dual role of behaving as a supercapacitor and a touch sensor whereas the bottom panel behaves as triboelectric nanogenerators (TENGs). These two devices are coupled using a rectifying bridge circuit to realize all-in-one self-charging power systems (Fig. 15a). The TENG device converts mechanical motions into electrical energy and stores it in rapidly charging supercapacitor devices. The stored energy can be later utilized for driving any wearable and portable electronic gadgets or sensors without any external power supplies. Fig. 15b shows the voltage *versus* time curve of the TENG device for various applied forces and frequencies and further compares the performance with that of reference ITO electrodes. The device exhibits excellent performance with low charge leakage while loading and unloading the forces in repeated cycles.[141] The integration of an ultra-low-power-consuming strain sensor with a supercapacitor and TENG device resulted in a self-powered strain monitoring system.[142] The active material for fabricating all three functional devices is AgNWs/PEDOT:PSS/PU. Fig. 15c shows an electrical circuit diagram integrating the strain sensor with SC and TENG devices. The transparency of the device is evident from the photograph shown in Fig. 15d. The device is useful in monitoring a wide range of human skin strains, including breathing and coughing (Fig. 15e and f).[142] In another example, a skin attachable strain sensor (SS) is integrated with a flexible transparent micro-supercapacitor (MSC) which possesses a fractal structure to ensure high stretchability.[143] The carbon nanotubes coated with MnO_2 in combination with a 1-butyl-3-methyl-imidazoliumbis(trifluoromethylsulfonyl)imide/poly(methyl methacrylate) electrolyte serve as an electrode for MSCs (Fig. 15g).
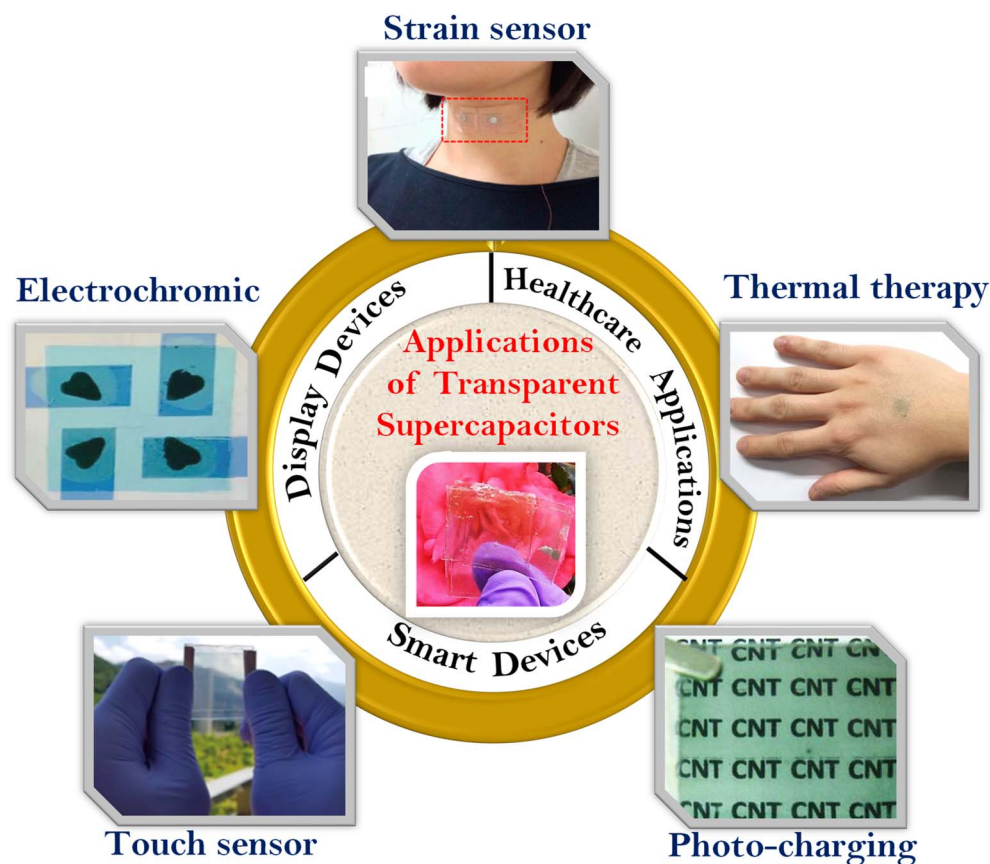

Fig. 16 Schematic representation highlighting the requirement of transparent supercapacitors as an energy storage device for various flexible transparent devices. Strain sensor – the photograph of a self-powered strain sensor composed of an AgNW/PEDOT:PSS/PU nanocomposite integrated with a supercapacitor, and a triboelectric nanogenerator. Reproduced with permission from ref. 142. Copyright 2015 American Chemical Society. Thermal therapy – a photograph of a transparent, flexible CuZr NTs–AgNW based hybrid supercapacitor for thermal therapy. Reproduced with permission from ref. 148. Copyright 2020 American Chemical Society. Photo-charging – the photograph of a transparent PANI/CNT polymer supercapacitor for photo-charging applications. Reproduced with permission from ref. 147. Copyright 2015 American Chemical Society. Touch sensor – a photograph of a single-layer graphene-based multifunctional supercapacitor device for self-charging and touch sensing. Reproduced with permission from ref. 141. Copyright 2019 American Chemical Society. Electrochromic – picture depicting the operation of four heart shaped totally independent energy-storing photovoltaics integrated with electrochromic supercapacitors under AM 1.5 G light. Reproduced with permission from ref. 139. Copyright 2020 by John Wiley and Sons.

4932 | *J. Mater. Chem. A*, 2023, **11**, 4907–4936

This journal is © The Royal Society of Chemistry 2023

The fabricated MSC offers ~80% transmittance with 12.6 mF cm^{-2} areal capacitance (see Fig. 15h). Interestingly, the change in the resistance of an AgNW based SS device while monitoring the pulse rate gives the same values when tested using a constant applied voltage (0.8 V) or with a MSC.[143] Due to the possible switching between completely transparent and dark-colored states, integrating electrochromic properties with energy storage in a single device is made possible, allowing fine control of light and heat through the window while simultaneously powering any low-power household electronics. Researchers have also designed electrochromic supercapacitors that provide an optical indicator of the charge stored in a supercapacitor by optical modulation from a fully charged colored state to a discharged transparent state.[144–146] An electrochromic supercapacitor shows various colors during the charging and discharging process and finds numerous applications such as displays, energy-saving smart windows, *etc*. The conducting polyaniline, an organic polymer, is a more common material used for this purpose because of its simple synthesis, cost-effectiveness, stability, and so on.[144] Cho *et al.* fabricated an energy-storing functional photovoltaic device that can harvest solar energies and store it as electrical energy (see the circuit diagram in Fig. 15i).[139] This multifunctional energy system is developed by monolithically integrating semi-transparent OPVs with electrochromic supercapacitors. The stored electrical energy can be a power source for various electronic gadgets like LEDs, sensors, *etc*. The image illustrates the operation of a red LED (1.8 V) using the energy stored in functional photovoltaics (Fig. 15i). The usage of an active electrochromic material helps by visually guiding the level of energy stored.[139] In another instance, conducting polyaniline polymers in combination with CNTs/ITO have been used for demonstrating the self-charging behavior of supercapacitors while illuminated with a light source (Fig. 15j and k). More importantly, this photo-charging effect of the supercapacitor occurs with no external bias.[147] In another report, a transparent supercapacitor is integrated with transparent electrodes to develop wirelessly rechargeable skin heat patches. Fig. 15l schematically shows the integration of a supercapacitor with an antenna, a diode, and capacitors to introduce wireless operation in the device. Fig. 15m illustrates the circuit diagram of the heat patch. On charging, the switch remains open and the AC power applied is rectified to DC power. In contrast, when discharging occurs, the switch is closed, and the stored energy from the supercapacitor is directed to the antenna to produce heat. The system remains robust for multiple cycles of charging and discharging.[148] Furthermore, a schematic diagram clearly showing the vital requirements of transparent supercapacitors for integrating in various transparent devices is shown in Fig. 16. The electrochromic transparent supercapacitors that exhibit complete transparent and dark states are rarely observed in the literature, and such devices can be very crucial for energy-efficient windows for specifically controlling the light and heat as an added functionality.[149,150] Presently, many electrochromic materials exhibit either a blue or a green color and are not completely transparent in the bleached state, thus restricting the complete advantage in window applications where transparency is necessary for visual appeal.

5. Closing remarks and future prospects

Due to enormous research activities, transparent electrodes for energy storage devices have been successfully developed over the last two decades. Supercapacitors are vital among many energy storage systems because of their excellent performance. Under persistent efforts, many electrode materials like graphene, CNTs, organic thin films, metal oxides, MXenes, MOFs, and metal nanowire networks, including hybrid electrodes, have been explored even with new device designs and configurations. However, desirable transparency and electrochemical performance with low-cost materials and methods for large-scale production challenge the practical application of transparent supercapacitors. Due to the existing trade-off between transmittance and capacitance, novel approaches are being developed to achieve high transparency (>90%) with high capacitance for modern transparent electronics. Instead of conventional device configurations, 3D-printed supercapacitors are gaining attention. Furthermore, modification approaches like developing electrodes on both sides of the separator substrate not only increase transmittance but also reduce the usage of unessential components. The requirement/specification of transmittance and desired capacitance usually depends on the application. For example, in the case of a transparent display, the desired transparency is usually aimed at ~90%, and the capacitance is optimized accordingly with an appropriate choice of electrode material. However, for applications such as large-area smart windows with electrochromic properties, the transmittance can be compromised up to ~70% while augmenting the areal-specific capacitance. The transparent supercapacitor is integrated with an electrochromic display, and the optical modulation serves as an indicator for the charging–discharging of the supercapacitor. Despite many significant developments, the status of transparent supercapacitors still needs to catch up to the practical commercial applications in transparent electronics. Besides transparency, accomplishing multiple functionalities like flexibility, stretchability, and self-healable properties is in demand. Finally, it is realized that continuous efforts are needed to improve the performance and introduce special functions in transparent energy storage devices for futuristic multifunctional transparent wearable electronic gadgets.

Conflicts of interest

There are no conflicts to declare.

Acknowledgements

This journal is © The Royal Society of Chemistry 2023

J. Mater. Chem. A, 2023, **11**, 4907–4936 | **4933**

References

1 L. Wang and X. Hu, *Batteries Supercaps*, 2020, **3**, 1275–1286.

2 R. G. Gordon, *MRS Bull.*, 2000, **25**, 52–57.

3 M. Mativenga, D. Geng, B. Kim and J. Jang, *ACS Appl. Mater. Interfaces*, 2015, **7**, 1578–1585.

4 W. Zhao, M. Jiang, W. Wang, S. Liu, W. Huang and Q. Zhao, *Adv. Funct. Mater.*, 2021, **31**, 2009136.

5 J. Jiang, B. Bao, M. Li, J. Sun, C. Zhang, Y. Li, F. Li, X. Yao and Y. Song, *Adv. Mater.*, 2016, **28**, 1420–1426.

6 D. Khim, G. S. Ryu, W. T. Park, H. Kim, M. Lee and Y. Y. Noh, *Adv. Mater.*, 2016, **28**, 2752–2759.

7 C. Zou, A. Komar, S. Fasold, J. Bohn, A. A. Muravsky, A. A. Murauski, T. Pertsch, D. N. Neshev and I. Staude, *ACS Photonics*, 2019, **6**, 1533–1540.

8 J. Chen, Y. Wang, W. Liu and Y. Ma, *ChemNanoMat*, 2020, **6**, 42–52.

9 J. Li, Q. Jiang, N. Yuan and J. Tang, *Materials*, 2018, **11**, 2280.

10 E. Navarrete-Astorga, J. Rodríguez-Moreno, E. A. Dalchiele, R. Schrebler, P. Leyton, J. R. Ramos-Barrado and F. Martín, *J. Solid State Electrochem.*, 2017, **21**, 1431–1444.

11 P. Simon and Y. Gogotsi, *Nat. Mater.*, 2008, **7**, 845–854.

12 J. R. Miller and P. Simon, *Science*, 2008, **321**, 651–652.

13 Y. Z. Zhang, Y. Wang, T. Cheng, L. Q. Yao, X. Li, W. Y. Lai and W. Huang, *Chem. Soc. Rev.*, 2019, **48**, 3229–3264.

14 W. K. Chee, H. N. Lim, Z. Zainal, N. M. Huang, I. Harrison and Y. Andou, *J. Phys. Chem. C*, 2016, **120**, 4153–4172.

15 H. Guo, Y. J. Tan, G. Chen, Z. Wang, G. J. Susanto, H. H. See, Z. Yang, Z. W. Lim, L. Yang and B. C. K. Tee, *Nat. Commun.*, 2020, **11**, 5747.

16 Y. Lee, J. Park, A. Choe, S. Cho, J. Kim and H. Ko, *Adv. Funct. Mater.*, 2020, **30**, 1904523.

17 P. Wang, M. Hu, H. Wang, Z. Chen, Y. Feng, J. Wang, W. Ling and Y. Huang, *Adv. Sci.*, 2020, **7**, 2001116.

18 Q. Liu, Z. Liu, C. Li, K. Xie, P. Zhu, B. Shao, J. Zhang, J. Yang, J. Zhang, Q. Wang and C. F. Guo, *Adv. Sci.*, 2020, **7**, 2000348.

19 Y. Gu, T. Zhang, H. Chen, F. Wang, Y. Pu, C. Gao and S. Li, *Nanoscale Res. Lett.*, 2019, **14**, 263.

20 D. Zhao, Y. Zhu, W. Cheng, W. Chen, Y. Wu and H. Yu, *Adv. Mater.*, 2020, **33**, 2000619.

21 N. Kurra, S. Kiruthika and G. U. Kulkarni, *RSC Adv.*, 2014, **4**, 20281–20289.

22 Z. Fan, *IOP Conf. Ser.: Mater. Sci. Eng.*, 2020, **772**, 012107.

23 S. Palchoudhury, K. Ramasamy, R. K. Gupta and A. Gupta, *Front. Mater.*, 2019, **5**, 83.

24 C. (John) Zhang, T. M. Higgins, S. H. Park, S. E. O'Brien, D. Long, J. N. Coleman and V. Nicolosi, *Nano Energy*, 2016, **28**, 495–505.

25 T. M. Higgins and J. N. Coleman, *ACS Appl. Mater. Interfaces*, 2015, **7**, 16495–16506.

26 A. M. Smith and S. Nie, *Acc. Chem. Res.*, 2010, **43**, 190–200.

27 G. Bahuguna, P. Ram, R. K. Sharma and R. Gupta, *ChemElectroChem*, 2018, **5**, 2767–2773.

28 R. Gupta, K. D. M. Rao, S. Kiruthika and G. U. Kulkarni, *ACS Appl. Mater. Interfaces*, 2016, **8**, 12559–12575.

29 G. Bahuguna, S. Chaudhary, R. K. Sharma and R. Gupta, *Energy Technol.*, 2019, **7**, 1900667.

30 A. B. Urgunde, G. Bahuguna, A. Dhamija, P. P. Das and R. Gupta, *ACS Appl. Electron. Mater.*, 2020, **2**, 3178–3186.

31 R. Gupta and T. S. Fisher, *Energy Technol.*, 2016, **5**, 740–746.

32 J. Pu, X. Wang, R. Xu, S. Xu and K. Komvopoulos, *Microsyst. Nanoeng.*, 2018, **4**, 16.

33 J. R. Gribbin, *Q Is for Quantum: An Encyclopedia of Particle Physics*, New York, Touchstone, 2000.

34 A. M. Ganose and D. O. Scanlon, *J. Mater. Chem. C*, 2016, **4**, 1467–1475.

35 G. Brunin, F. Ricci, V. A. Ha, G. M. Rignanese and G. Hautier, *npj Comput. Mater.*, 2019, **5**, 63.

36 P. J. King, T. M. Higgins, S. De, N. Nicoloso and J. N. Coleman, *ACS Nano*, 2012, **6**, 1732–1741.

37 C. (John) Zhang and V. Nicolosi, *Energy Storage Mater.*, 2019, **16**, 102–125.

38 R. M. Mutiso, M. C. Sherrott, A. R. Rathmell, B. J. Wiley and K. I. Winey, *ACS Nano*, 2013, **7**, 7654–7663.

39 C. J. Zhang, B. Anasori, A. Seral-Ascaso, S. H. Park, N. McEvoy, A. Shmeliov, G. S. Duesberg, J. N. Coleman, Y. Gogotsi and V. Nicolosi, *Adv. Mater.*, 2017, **29**, 1702678.

40 X. Jiao, C. Zhang and Z. Yuan, *ACS Appl. Mater. Interfaces*, 2018, **10**, 41299–41311.

41 J. L. Xu, Y. H. Liu, X. Gao, Y. Sun, S. Shen, X. Cai, L. Chen and S. D. Wang, *ACS Appl. Mater. Interfaces*, 2017, **9**, 27649–27656.

42 N. Li, G. Yang, Y. Sun, H. Song, H. Cui, G. Yang and C. Wang, *Nano Lett.*, 2015, **15**, 3195–3203.

43 Y. Chen, J. Ma, M. Xu and S. Liu, *Nano Today*, 2020, **35**, 100976.

44 H. Lee, S. Hong, J. Lee, Y. D. Suh, J. Kwon, H. Moon, H. Kim, J. Yeo and S. H. Ko, *ACS Appl. Mater. Interfaces*, 2016, **8**, 15449–15458.

45 J. Yang, T. Hong, J. Deng, Y. Wang, F. Lei, J. Zhang, B. Yu, Z. Wu, X. Zhang and C. F. Guo, *Chem. Commun.*, 2019, **55**, 13737–13740.

46 S. Bellani, L. Najafi, G. Tullii, A. Ansaldo, R. Oropesa-Nuñez, M. Prato, M. Colombo, M. R. Antognazza and F. Bonaccorso, *J. Mater. Chem. A*, 2017, **5**, 25177–25186.

47 T. G. Yun, M. Park, D. H. Kim, D. Kim, J. Y. Cheong, J. G. Bae, S. M. Han and I. D. Kim, *ACS Nano*, 2019, **13**, 3141–3150.

48 A. Kumar and C. Zhou, *ACS Nano*, 2010, **4**, 11–14.

49 G. U. Kulkarni, S. Kiruthika, R. Gupta and K. D. M. Rao, *Curr. Opin. Chem. Eng.*, 2015, **8**, 60–68.

50 S. R. C. Vivekchand, R. Chandra Sekhar, A. Govindaraj and C. N. R. Rao, *J. Chem. Sci.*, 2008, **120**, 9–13.

51 K. S. Novoselov, A. K. Geim, S. V. Morozov, D. Jiang, Y. Zhang, S. V. Dubonos, I. V. Grigorieva and A. A. Firsov, *Science*, 2004, **306**, 666–669.

52 K. S. Novoselov, V. I. Fal'Ko, L. Colombo, P. R. Gellert, M. G. Schwab and K. Kim, *Nature*, 2012, **490**, 192–200.

53 J. Xia, F. Chen, J. Li and N. Tao, *Nat. Nanotechnol.*, 2009, **4**, 505–509.

4934 | *J. Mater. Chem. A*, 2023, **11**, 4907–4936

This journal is © The Royal Society of Chemistry 2023

54 S. Guo and S. Dong, *Chem. Soc. Rev.*, 2011, **40**, 2644–2672.

55 A. Yu, I. Roes, A. Davies and Z. Chen, *Appl. Phys. Lett.*, 2010, **96**, 253105.

56 H. Peng, Y. Zhong, X. Zhang, Y. He and G. Wang, *Langmuir*, 2018, **34**, 15245–15252.

57 K. Jo, S. Lee, S. M. Kim, J. Bin In, S. M. Lee, J. H. Kim, H. J. Lee and K. S. Kim, *Chem. Mater.*, 2015, **27**, 3621–3627.

58 E. O. Polat and C. Kocabas, *Nano Lett.*, 2013, **13**, 5851–5857.

59 X. Fan, T. Chen and L. Dai, *RSC Adv.*, 2014, **4**, 36996–37002.

60 P. Xu, J. Kang, J. B. Choi, J. Suhr, J. Yu, F. Li, J. H. Byun, B. S. Kim and T. W. Chou, *ACS Nano*, 2014, **8**, 9437–9445.

61 Y. Chen, X. Y. Fu, Y. Y. Yue, N. Zhang, J. Feng and H. B. Sun, *Appl. Surf. Sci.*, 2019, **467–468**, 104–111.

62 Q. A. Sial, M. S. Javed, Y. J. Lee, L. T. Duy and H. Seo, *Ceram. Int.*, 2020, **46**, 23145–23154.

63 Y. Gao, Y. S. Zhou, W. Xiong, L. J. Jiang, M. Mahjouri-Samani, P. Thirugnanam, X. Huang, M. M. Wang, L. Jiang and Y. F. Lu, *APL Mater.*, 2013, **1**, 012101.

64 M. Z. Rahman and T. Edvinsson, *J. Mater. Chem. A*, 2020, **8**, 8234–8237.

65 J. Cárdenas-Martínez, B. L. España-Sánchez, R. Esparza and J. A. Ávila-Niño, *Synth. Met.*, 2020, **267**, 116436.

66 L. V. Kayser and D. J. Lipomi, *Adv. Mater.*, 2019, **31**, 1806133.

67 H. Yan and H. Okuzaki, *Synth. Met.*, 2009, **159**, 2225–2228.

68 T. Cheng, Y. Z. Zhang, J. P. Yi, L. Yang, J. D. Zhang, W. Y. Lai and W. Huang, *J. Mater. Chem. A*, 2016, **4**, 13754–13763.

69 R. T. Ginting, M. M. Ovhal and J. W. Kang, *Nano Energy*, 2018, **53**, 650–657.

70 S. B. Singh, T. Kshetri, T. I. Singh, N. H. Kim and J. H. Lee, *Chem. Eng. J.*, 2019, **359**, 197–207.

71 J. Xu, D. Wang, L. Fan, Y. Yuan, W. Wei, R. Liu, S. Gu and W. Xu, *Org. Electron.*, 2015, **26**, 292–299.

72 W. Xiong, X. Hu, X. Wu, Y. Zeng, B. Wang, G. He and Z. Zhu, *J. Mater. Chem. A*, 2015, **3**, 17209–17216.

73 Y. Hu, Y. Zhao, Y. Li, H. Li, H. Shao and L. Qu, *Electrochim. Acta*, 2012, **66**, 279–286.

74 Y. Huang, H. Li, Z. Wang, M. Zhu, Z. Pei, Q. Xue, Y. Huang and C. Zhi, *Nano Energy*, 2016, **22**, 422–438.

75 I. Shown, A. Ganguly, L. C. Chen and K. H. Chen, *Energy Sci. Eng.*, 2015, **3**, 2–26.

76 H. Moon, H. Lee, J. Kwon, Y. D. Suh, D. K. Kim, I. Ha, J. Yeo, S. Hong and S. H. Ko, *Sci. Rep.*, 2017, **7**, 41981.

77 D. Wei, S. J. Wakeham, T. W. Ng, M. J. Thwaites, H. Brown and P. Beecher, *Electrochem. Commun.*, 2009, **11**, 2285–2287.

78 X. Y. Liu, Y. Q. Gao and G. W. Yang, *Nanoscale*, 2016, **8**, 4227–4235.

79 F. Moser, L. Athouël, O. Crosnier, F. Favier, D. Bélanger and T. Brousse, *Electrochem. Commun.*, 2009, **11**, 1259–1261.

80 Y. Hu, H. Zhu, J. Wang and Z. Chen, *J. Alloys Compd.*, 2011, **509**, 10234–10240.

81 J. Choi, D. Nam, D. Shin, Y. Song, C. H. Kwon, I. Cho, S. W. Lee and J. Cho, *ACS Nano*, 2019, **13**, 12719–12731.

82 I. Ryu, M. Yang, H. Kwon, H. K. Park, Y. R. Do, S. B. Lee and S. Yim, *Langmuir*, 2014, **30**, 1704–1709.

83 J. Rodríguez, E. Navarrete, E. A. Dalchiele, L. Sánchez, J. R. Ramos-Barrado and F. Martín, *J. Power Sources*, 2013, **237**, 270–276.

84 P. C. Chen, G. Shen, S. Sukcharoenchoke and C. Zhou, *Appl. Phys. Lett.*, 2009, **94**, 043113.

85 V. Q. Le, P. A. Le, S. C. Wu, Y. H. Lai, Y. G. Lin, K. H. Wei, Y. H. Chu and Y. L. Chueh, *Small*, 2020, **16**, 2000020.

86 B. Yao, L. Huang, J. Zhang, X. Gao, J. Wu, Y. Cheng, X. Xiao, B. Wang, Y. Li and J. Zhou, *Adv. Mater.*, 2016, **28**, 6353–6358.

87 M. W. Barsoum, *Prog. Solid State Chem.*, 2000, **28**, 201–281.

88 M. Naguib, M. Kurtoglu, V. Presser, J. Lu, J. Niu, M. Heon, L. Hultman, Y. Gogotsi and M. W. Barsoum, *Adv. Mater.*, 2011, **23**, 4248–4253.

89 P. Salles, E. Quain, N. Kurra, A. Sarycheva and Y. Gogotsi, *Small*, 2018, **14**, 1802864.

90 J. Halim, M. R. Lukatskaya, K. M. Cook, J. Lu, C. R. Smith, L. Å. Näslund, S. J. May, L. Hultman, Y. Gogotsi, P. Eklund and M. W. Barsoum, *Chem. Mater.*, 2014, **26**, 2374–2381.

91 K. Hantanasirisakul, M. Q. Zhao, P. Urbankowski, J. Halim, B. Anasori, S. Kota, C. E. Ren, M. W. Barsoum and Y. Gogotsi, *Adv. Electron. Mater.*, 2016, **2**, 1600050.

92 L. Qin, J. Jiang, Q. Tao, C. Wang, I. Persson, M. Fahlman, P. O. A. Persson, L. Hou, J. Rosen and F. Zhang, *J. Mater. Chem. A*, 2020, **8**, 5467–5475.

93 G. Wu, J. Huang, Y. Zang, J. He and G. Xu, *J. Am. Chem. Soc.*, 2017, **139**, 1360–1363.

94 D. Sheberla, L. Sun, M. A. Blood-forsythe, S. Er, C. R. Wade and C. K. Brozek, *J. Am. Chem. Soc.*, 2014, **136**, 8859.

95 W. Zhao, T. Chen, W. Wang, B. Jin, J. Peng, S. Bi, M. Jiang, S. Liu, Q. Zhao and W. Huang, *Sci. Bull.*, 2020, **65**, 1803–1811.

96 S. Gong, Y. Zhao, Q. Shi, Y. Wang, L. W. Yap and W. Cheng, *Electroanalysis*, 2016, **28**, 1298–1304.

97 H. Sheng, X. Zhang, Y. Ma, P. Wang, J. Zhou, Q. Su, W. Lan, E. Xie and C. J. Zhang, *ACS Appl. Mater. Interfaces*, 2019, **11**, 8992–9001.

98 X. Liu, D. Li, X. Chen, W. Y. Lai and W. Huang, *ACS Appl. Mater. Interfaces*, 2018, **10**, 32536–32542.

99 J. Liu, G. Shen, S. Zhao, X. He, C. Zhang, T. Jiang, J. Jiang and B. Chen, *J. Mater. Chem. A*, 2019, **7**, 8184–8193.

100 H.-Z. Geng, K. K. Kim, K. P. So, Y. S. Lee, Y. Chang and Y. H. Lee, *J. Am. Chem. Soc.*, 2007, **129**, 7758–7759.

101 L. Xiao, Z. Chen, C. Feng, L. Liu, Z. Q. Bai, Y. Wang, L. Qian, Y. Zhang, Q. Li, K. Jiang and S. Fan, *Nano Lett.*, 2008, **8**, 4539–4545.

102 D. Zhang, K. Ryu, X. Liu, E. Polikarpov, M. Tompson and C. Zhou, *Nano Lett.*, 2006, **6**, 1880–1886.

103 W. Ma, L. Song, R. Yang, T. Zhang, Y. Zhao, L. Sun, Y. Ren, D. Liu, L. Liu, J. Shen, Z. Zhang, Y. Xiang, W. Zhou and S. S. Xie, *Nano Lett.*, 2007, **7**, 2307–2311.

104 Z. Niu, W. Zhou, J. Chen, G. Feng, H. Li, Y. Hu, W. Ma, H. Dong, J. Li and S. Xie, *Small*, 2013, **9**, 518–524.

105 E. Senokos, M. Rana, M. Vila, J. Fernandez-Cestau, R. D. Costa, R. Marcilla and J. J. Vilatela, *Nanoscale*, 2020, **12**, 16980–16986.

106 R. Yuksel, Z. Sarioba, A. Cirpan, P. Hiralal and H. E. Unalan, *ACS Appl. Mater. Interfaces*, 2014, **6**, 15434–15439.

This journal is © The Royal Society of Chemistry 2023

J. Mater. Chem. A, 2023, **11**, 4907–4936 | **4935**

107 P. Kanninen, N. D. Luong, L. H. Sinh, I. V. Anoshkin, A. Tsapenko, J. Seppälä, A. G. Nasibulin and T. Kallio, *Nanotechnology*, 2016, **27**, 235403.

108 T. Chen, H. Peng, M. Durstock and L. Dai, *Sci. Rep.*, 2014, **4**, 1–7.

109 J. Ge, G. Cheng and L. Chen, *Nanoscale*, 2011, **3**, 3084–3088.

110 J. Chen, W. Xiao, T. Hu, P. Chen, T. Lan, P. Li, Y. Li, B. Mi and Y. Ma, *ACS Appl. Mater. Interfaces*, 2020, **12**, 5885–5891.

111 H. Lin, L. Li, J. Ren, Z. Cai, L. Qiu, Z. Yang and H. Peng, *Sci. Rep.*, 2013, **3**, 1353.

112 S. An, H. S. Jo, D. Y. Kim, H. J. Lee, B. K. Ju, S. S. Al-Deyab, J. H. Ahn, Y. Qin, M. T. Swihart, A. L. Yarin and S. S. Yoon, *Adv. Mater.*, 2016, **28**, 7149–7154.

113 C. S. Kwak, T. H. Ko, J. H. Lee, H. Y. Kim and B. S. Kim, *ACS Appl. Energy Mater.*, 2020, **3**, 2394–2403.

114 S. B. Singh, T. I. Singh, N. H. Kim and J. H. Lee, *J. Mater. Chem. A*, 2019, **7**, 10672–10683.

115 Y. Lee, S. Chae, H. Park, J. Kim and S. H. Jeong, *Chem. Eng. J.*, 2020, **382**, 122798.

116 B. S. Soram, I. S. Thangjam, J. Y. Dai, T. Kshetri, N. H. Kim and J. H. Lee, *Chem. Eng. J.*, 2020, **395**, 125019.

117 T. Qiu, B. Luo, M. Giersig, E. M. Akinoglu, L. Hao, X. Wang, L. Shi, M. Jin and L. Zhi, *Small*, 2014, **10**, 4136–4141.

118 C. F. Guo, T. Sun, Q. Liu, Z. Suo and Z. Ren, *Nat. Commun.*, 2014, **5**, 3121.

119 Y. Wang, W. Zhou, Q. Kang, J. Chen, Y. Li, X. Feng, D. Wang, Y. Ma and W. Huang, *ACS Appl. Mater. Interfaces*, 2018, **10**, 27001–27008.

120 T. Liu, R. Yan, H. Huang, L. Pan, X. Cao, A. deMellollo and M. Niederberger, *Adv. Funct. Mater.*, 2020, **30**, 2004410.

121 Y. H. Liu, J. L. Xu, X. Gao, Y. L. Sun, J. J. Lv, S. Shen, L. Sen Chen and S. D. Wang, *Energy Environ. Sci.*, 2017, **10**, 2534–2543.

122 Y. H. Liu, J. L. Xu, S. Shen, X. L. Cai, L. Sen Chen and S. D. Wang, *J. Mater. Chem. A*, 2017, **5**, 9032–9041.

123 Y. H. Liu, Z. Y. Jiang and J. L. Xu, *ACS Appl. Mater. Interfaces*, 2019, **11**, 24047–24056.

124 B. Han, K. Pei, Y. Huang, X. Zhang, Q. Rong, Q. Lin, Y. Guo, T. Sun, C. Guo, D. Carnahan, M. Giersig, Y. Wang, J. Gao, Z. Ren and K. Kempa, *Adv. Mater.*, 2014, **26**, 873–877.

125 S. Kiruthika, C. Sow and G. U. Kulkarni, *Small*, 2017, **13**, 1701906.

126 S. Kiruthika, R. Gupta, A. Anand, A. Kumar and G. U. Kulkarni, *ACS Appl. Mater. Interfaces*, 2015, **7**, 27215–27222.

127 S. Kiruthika, R. Gupta and G. U. Kulkarni, *RSC Adv.*, 2014, **4**, 49745–49751.

128 R. Gupta, K. D. M. Rao, K. Srivastava, A. Kumar, S. Kiruthika and G. U. Kulkarni, *ACS Appl. Mater. Interfaces*, 2014, **6**, 13688–13696.

129 S. Kiruthika, R. Gupta, K. D. M. Rao, S. Chakraborty, N. Padmavathy and G. U. Kulkarni, *J. Mater. Chem. C*, 2014, **2**, 2089–2094.

130 R. Gupta, K. D. M. Rao and G. U. Kulkarni, *RSC Adv.*, 2014, **4**, 31108–31112.

131 B. S. Soram, J. Y. Dai, I. S. Thangjam, N. H. Kim and J. H. Lee, *J. Mater. Chem. A*, 2020, **8**, 24040–24052.

132 A. K. Singh, R. K. Govind, S. Kiruthika, M. G. Sreenivasan and G. U. Kulkarni, *Mater. Chem. Phys.*, 2020, **239**, 121997.

133 I. Mondal, S. Kiruthika, M. K. Ganesha, M. Baral, A. Kumar, S. Vimala, P. L. Madhuri, G. G. Nair, S. K. Prasad, A. K. Singh and G. U. Kulkarni, *J. Mater. Chem. A*, 2021, **9**, 23157–23168.

134 B. Xie, Y. Wang, W. Lai, W. Lin, Z. Lin, Z. Zhang, P. Zou, Y. Xu, S. Zhou, C. Yang, F. Kang and C. P. Wong, *Nano Energy*, 2016, **26**, 276–285.

135 S. Sollami Delekta, A. D. Smith, J. Li and M. Östling, *Nanoscale*, 2017, **9**, 6998–7005.

136 J. Li, Q. Shi, Y. Shao, C. Hou, Y. Li, Q. Zhang and H. Wang, *Energy Storage Mater.*, 2019, **16**, 212–219.

137 H. Li, Q. Zhao, W. Wang, H. Dong, D. Xu, G. Zou, H. Duan and D. Yu, *Nano Lett.*, 2013, **13**, 1271–1277.

138 R. Gupta, S. Walia, M. Hösel, J. Jensen, D. Angmo, F. C. Krebs and G. U. Kulkarni, *J. Mater. Chem. A*, 2014, **2**, 10930–10937.

139 J. Cho, T. Y. Yun, H. Y. Noh, S. H. Baek, M. Nam, B. Kim, H. C. Moon and D. H. Ko, *Adv. Funct. Mater.*, 2020, **30**, 1909601.

140 P. Salles, D. Pinto, K. Hantanasirisakul, K. Maleski, C. E. Shuck and Y. Gogotsi, *Adv. Funct. Mater.*, 2019, **29**, 1809223.

141 S. Chun, W. Son, G. Lee, S. H. Kim, J. W. Park, S. J. Kim, C. Pang and C. Choi, *ACS Appl. Mater. Interfaces*, 2019, **11**, 9301–9308.

142 B. U. Hwang, J. H. Lee, T. Q. Trung, E. Roh, D. il Kim, S. W. Kim and N. E. Lee, *ACS Nano*, 2015, **9**, 8801–8810.

143 J. Yun, H. Lee, C. Song, Y. R. Jeong, J. W. Park, J. H. Lee, D. S. Kim, K. Keum, M. S. Kim, S. W. Jin, Y. H. Lee, J. W. Kim, G. Zi and J. S. Ha, *Chem. Eng. J.*, 2020, **387**, 124076.

144 S. Kiruthika and G. U. Kulkarni, *Energy Technol.*, 2020, **8**, 1901364.

145 D. Wei, M. R. J. Scherer, C. Bower, P. Andrew, T. Ryhänen and U. Steiner, *Nano Lett.*, 2012, **12**, 1857–1862.

146 S. Xie, S. Chen, Z. Bi, S. Jia, X. Guo, X. Gao and X. Li, *Chem. Eng. J.*, 2019, **370**, 1459–1466.

147 Y. Yin, K. Feng, C. Liu and S. Fan, *J. Phys. Chem. C*, 2015, **119**, 8488–8491.

148 S. Lee, S. W. Kim, M. Ghidelli, H. S. An, J. Jang, A. L. Bassi, S. Y. Lee and J. U. Park, *Nano Lett.*, 2020, **20**, 4872–4881.

149 Q. Guo, X. Zhao, Z. Li, B. Wang, D. Wang and G. Nie, *ACS Appl. Energy Mater.*, 2020, **3**, 2727–2736.

150 H. Wang, C. J. Yao, H. J. Nie, L. Yang, S. Mei and Q. Zhang, *J. Mater. Chem. C*, 2020, **8**, 15507–15525.

4936 | *J. Mater. Chem. A*, 2023, **11**, 4907–4936

This journal is © The Royal Society of Chemistry 2023